Materials Advances

ROYAL SOCIETY OF CHEMISTRY

PAPER

View Article Online
View Journal | View Issue

Check for updates

Cite this: *Mater. Adv.*, 2025, 6, 2211

Engineered flexible microsupercapacitors with MOF-derived Co_3O_4/rGO nanocomposite optimized *via* response surface methodology for enhanced energy storage†

Mohammad Saquib,[a] Shilpa Shetty,[a] S. G. Siddanth,[b] Nagaraja Nayak,[a] Chandra Sekhar Rout,[ce] Ramakrishna Nayak,[d] Ahipa T. N.[e] and M. Selvakumar*[a]

Received 14th November 2024,
Accepted 27th February 2025

DOI: 10.1039/d4ma01126k

rsc.li/materials-advances

A promising microsupercapacitor design was achieved by printing conductive ink composed of porous Co_3O_4 nanoparticles derived from ZIF-67 with *in situ* reduced graphene oxide (rGO) growth *via* thermal reduction. The symmetric micro-supercapacitor achieved an areal capacitance of 939 mF cm^{-2}, an energy density of 130.4 μW h cm^{-2}, and a power density of 2134 mW cm^{-2}, optimized *via* response surface methodology (RSM), with peak performance at 550 °C and a composite desirability of 86.48%. Additionally, it demonstrated exceptional cyclic stability, retaining 91.7% of its initial capacitance after 10 000 cycles of charge and discharge. The asymmetric device demonstrated even higher performance, with an areal capacitance of 1220.2 mF cm^{-2}, an energy density of 343.51 μW h cm^{-2}, and a power density of 3876.6 mW cm^{-2}, Similarly, the Co_3O_4/rGO-550 microsupercapacitor demonstrated 94.6% cycling stability even after 10 000 charge–discharge cycles, highlighting its durability and long-term performance.

Open Access Article. Published on 10 de març 2025. Downloaded on 17/5/2026 14:58:41.
This article is licensed under a Creative Commons Attribution 3.0 Unported Licence.

1. Introduction

Rising global energy demand highlights the urgent need for sustainable alternatives to depleting non-renewable resources like petrochemicals, fossil fuels, and natural gas. Exploration of alternative energy sources is crucial to meet future energy needs sustainably.[1] Recent research has targeted energy challenges through electrochemical reactions, and advancing devices like lithium-ion batteries, solar cells, electrolytic cells, and supercapacitors.[2,3] In the modern era, there is a shift towards compact, flexible, and portable electronic devices, emphasizing the need for flexible and wearable fabrication techniques.[4] In recent years, wearable electronics have emerged as a key technology for future generations. Flexible sensors, developed and integrated into everyday life, contribute substantially to this trend. The primary challenge is fabricating flexible devices with high power density and extended charge–discharge cycles.[5] There is a significant gap to be addressed by developing an economically friendly, flexible micro-supercapacitor with superior electrochemical performance. This requires optimizing ink formulations and fabricating devices to achieve enhanced performance. Zeolitic imidazole frameworks (ZIFs), a subclass of MOFs, offer great stability and large specific surface area but endure low electrical conductivity and chemical stability.[6] In order to subdue the aforementioned setbacks, researchers have developed MOF-derived materials through pyrolysis, converting MOFs into metal oxide nanoparticles with enhanced conductivity and surface area. These materials are often combined with carbonaceous materials to further improve their characteristics.

Unlike conventional supercapacitors (sandwich structure), microsupercapacitors typically adopt a planar design with interdigital electrodes.[2,7–11] This configuration allows electrolyte ions to move swiftly through the narrow interspaces between the interdigitated electrodes, enabling ultrahigh power density.[12,13] The in-plane interdigital architecture presents numerous merits over the traditional sandwich structure while sustaining stability over millions of cycles. Its most notable benefit is the gap between the electronically isolated interdigital electrodes, eliminating the desirability for a separator that is typically required in conventional sandwich-structured supercapacitors. Notably, by further

[a] Department of Chemistry, Manipal Institute of Technology, Manipal Academy of Higher Education, Manipal-576104, Karnataka, India. E-mail: selva.kumar@manipal.edu
[b] Department of Chemical Engineering, Manipal Institute of Technology, Manipal Academy of Higher Education, Manipal, Karnataka, 576104, India
[c] Department of Chemical Engineering, Chungbuk National University, Cheongju, Chungbuk 28644, Republic of Korea
[d] Department of Humanities and Management, Manipal Institute of Technology, Manipal Academy of Higher Education, Manipal, Karnataka, 576104, India
[e] Centre for Nano and Material Sciences, Jain (Deemed-to-be University), Jain Global Campus, Kanakapura, Bangalore, Karnataka, 562112, India

† Electronic supplementary information (ESI) available. See DOI: https://doi.org/10.1039/d4ma01126k

© 2025 The Author(s). Published by the Royal Society of Chemistry

Open Access Article. Published on 10 de març 2025. Downloaded on 17/5/2026 14:58:41.
This article is licensed under a Creative Commons Attribution 3.0 Unported Licence.

minimizing the separations between electrode fingers, the ion migration resistance is reduced, enhancing the frequency response characteristics and increasing power density. These advantages make microsupercapacitors integrated with an in-plane interdigital electrode architecture highly promising for use in miniaturized portable and wearable electronics, particularly in on-chip electronic devices.[14–16] Despite the relatively low specific capacitance of the Co_3O_4 owing to its volume changes and inferior diffusion capabilities of its conducting ions, it is still an affordable alternative with a compelling redox activity and high theoretical capacitance.[17,18] Integrating flexible microsupercapacitors with high-resolution integrated microelectrodes remains a significant challenge. Screen printing[8,19] has a high deposition rate, making it suitable for mass-producing printing of the micro supercapacitor as a capacitive energy storage device. Developing functional inks with suitable rheological properties is crucial for high-resolution screen printing. This study presents an ingenious approach for designing flexible microsupercapacitors by formulating a functional conductive ink that blends Co_3O_4 with carbon-based nanocomposite. The conductive ink is prepared through a simplified process involving single-step calcination of ZIF-67 to produce cobalt oxide (Co_3O_4) nanoparticles, followed by the addition of graphene oxide (GO), which is then thermally reduced *in situ* to form reduced graphene oxide (rGO) in an optimal ratio for microsupercapacitor fabrication. This methodology minimizes the stages incorporated in the formulation of the conductive nanocomposite-based ink with the supplemental benefit of producing functionalities analogous to commercially accessible alternatives. For the first time, we report nanocomposite-based electrode material (Co_3O_4@rGO-NC), which was utilized for the formulation of the functional ink for screen printing of flexible microsupercapacitor. The conductive ink formulated using Co_3O_4@rGO-NCs has excellent stability, viscosity, and printability.[20] The combined effect of Co_3O_4 nanoparticles and the rGO framework results in desirable characteristics such as high conductivity, well-distribution of nanoparticles, and architectures with enhanced porosity, ultimately enhancing the electrochemical performance of the microsupercapacitor. The performance of a microsupercapacitor is influenced by multiple operating parameters, including dopant concentration, surfactant concentration, pH, temperature, monomer concentration, electrode material composition, material thickness, and several other factors. In this response optimization study, temperature was selected as the primary input parameter to investigate its effects on the performance metrics of a symmetric supercapacitor. The key output parameters analysed were areal capacitance, energy density, and power density. Minitab 16 software was utilized to develop mathematical models and conduct statistical analyses of the experimental data. This systematic approach enabled the validation of the degree of correlation between the experimental results and model-predicted values.

2. Experimental section

2.1. Synthesis of nanoZIF-67

In the synthesis Procedure, a solution was prepared by dissolving 0.71 g of ($Co(NO_3)_2{\cdot}6H_2O$) and 1.62 g of $C_4H_6N_2$ in 50 mL of methanol at ~25 °C for approximately 15–20 minutes. The resulting mixture was subjected to stirring on a magnetic stirrer and allowed to react for 24 hours. Following the reaction, the purple-coloured solid product was separated using centrifugation and subsequently washed multiple times with methanol. To remove any residual solvent, the solid was then vacuum dried at 100 °C.[8,21] The obtained nanoZIF-67 was then composited with graphene oxide (GO) and subjected to calcination at five different temperatures which are 350 °C, 450 °C, 550 °C, 650 °C, and 750 °C. During this thermal reduction process, the ZIF/GO composite was converted into a black powder of Co_3O_4/rGO, accompanied by the loss of oxygen molecules. The calcination process facilitated the transformation of the ZIF-67 framework into Co_3O_4 while simultaneously reducing GO to reduced graphene oxide (rGO), resulting in a composite material as illustrated in Scheme 1.

2.2. Synthesis mechanism

The synthesis of Co_3O_4 using NanoZIF-67 as a precursor material involves a strategic annealing process at various temperatures to enhance its electrochemical performance. Initially, NanoZIF-67 is prepared by combining cobalt nitrate and 2-methylimidazole, forming a zeolitic imidazolate framework (ZIF-67). During synthesis, graphene oxide (GO) is introduced *in situ* to ensure its homogeneous distribution within the ZIF-67 structure. The composite material (GO-ZIF-67) then undergoes thermal reduction, converting GO into reduced graphene oxide (rGO) and initiating the formation of Co_3O_4. The annealing process is carried out at three different temperatures: 350 °C, 450 °C, and 550 °C, with the duration kept constant to isolate the effect of temperature variation. At 350 °C, the initial phase formation of Co_3O_4 begins with the oxidation of Co ions from ZIF-67, resulting in smaller, less defined pores and a moderate increase in surface area due to mild expansion. When annealed at 450 °C, the oxidation process is more pronounced, facilitating the growth of larger, more interconnected pores, significantly enhancing the surface area and contributing to improved electrochemical performance. At 550 °C, the optimal pore expansion is achieved, resulting in a highly porous structure with maximum surface area. The high temperature also promotes well-formed and stable Co_3O_4 crystallites, ensuring a highly conductive and electrochemically active material. The detailed reaction mechanism is shown in Scheme 2. Additionally, the thermal reduction of GO to rGO is completed, further increasing the conductivity and contributing to the overall electrochemical behaviour.[22,23]

2.3. Preparation of conductive nanocomposite inks

To formulate the inks containing porous Co_3O_4/rGO nanocomposites annealed at five different temperatures (CR-1, CR-2, CR-3, CR-4, and CR-5), a vehicle resin mixture was employed, comprising a solvent and a binder. Specifically, the mixture consisted of diacetone alcohol as the solvent, making up 85% of the total, and cellulose acetate propionate as the binder, accounting for the remaining 15%. The solvent and binder were mixed exhaustively by continuously stirring for one hour to

© 2025 The Author(s). Published by the Royal Society of Chemistry

Open Access Article. Published on 10 de març 2025. Downloaded on 17/5/2026 14:58:41.
This article is licensed under a Creative Commons Attribution 3.0 Unported Licence.

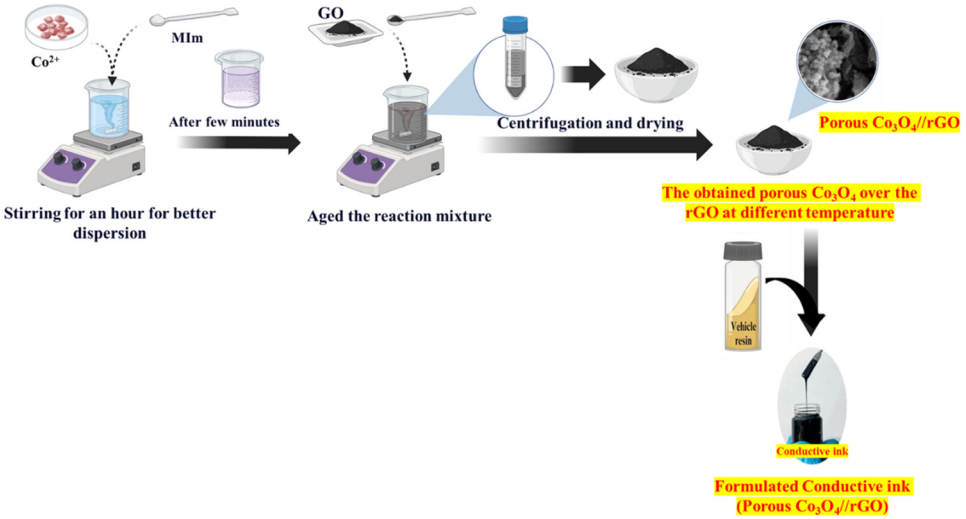

Scheme 1 Representation of the synthesis process of Co_3O_4/rGO and the ink formulation.

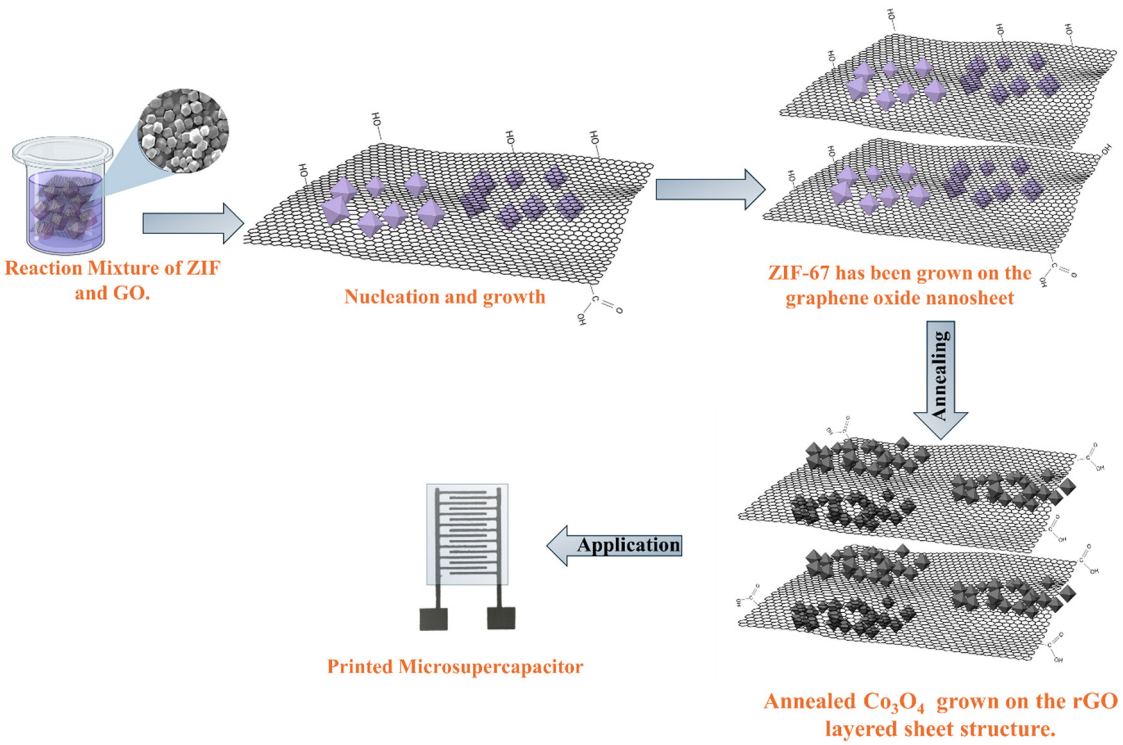

Scheme 2 Shows the mechanism of *in situ* growth of nanoparticles on the graphene sheet.

obtain a homogeneous solution. A suitable proportion of non-ionic surfactant was added to the mixture to attain the desired printability of the viscous conductive ink. The five nanocomposite inks thus formulated were employed for the screen printing and fabrication of flexible microsupercapacitors. These inks included CR-1 (Co_3O_4/rGO at 350 °C), CR-2 (Co_3O_4/rGO at 450 °C), CR-3 (Co_3O_4/rGO at 550 °C), CR-4 (Co_3O_4/rGO at 650 °C), and CR-5 (Co_3O_4/rGO at 750 °C) each designed to achieve specific compositions and properties suitable for the screen-printing technique.[24] Furthermore, the rheological properties of the inks were analysed, focusing on viscosity and the contact angle of the ink on the substrate. These measurements were conducted to evaluate the ink's flow characteristics and its interaction with the printing surface, ensuring the inks were optimized for the intended application.

2.4. Mechanism of MOF derived Co_3O_4 intercalated rGO matrix

The interaction between MOF-derived Co_3O_4 and reduced graphene oxide (rGO) during annealing is illustrated in Scheme 3.

Open Access Article. Published on 10 de març 2025. Downloaded on 17/5/2026 14:58:41.
This article is licensed under a Creative Commons Attribution 3.0 Unported Licence.

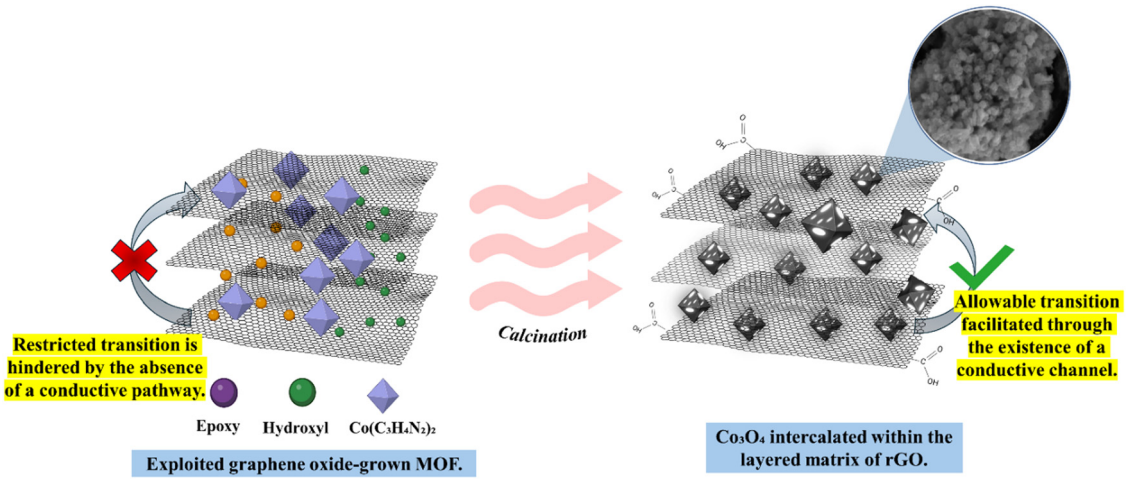

Scheme 3 Illustration of the interaction between MOF-derived Co_3O_4 and reduced graphene oxide (rGO) during annealing.

Co_3O_4 nanoparticles are intercalated within the layered rGO matrix through a calcination process conducted under an oxygen atmosphere. Initially, ZIF-67 nanocubes are grown on the graphene oxide (GO) matrix *via* a simple chemical precipitation reaction between the cobalt metal centres in $Co(C_3H_4N_2)_2$ complexes and the oxygen-containing functional groups in GO. This process, driven by electrostatic forces of attraction, results in the formation of strong Co–O–C bonds, effectively anchoring the ZIF-67 nanocubes to the GO layers. The ZIF-67-GO complex is then subjected to calcination at varying temperatures (350 °C to 750 °C), leading to the transformation of the GO–$Co(OH)_2$ precursor into an rGO–Co_3O_4 nanocomposite. During this process, the incorporation of Co_3O_4 nanoparticles within the rGO layers prevents the restacking of the rGO sheets, thus maintaining the structural integrity of the matrix. The calcination temperature plays a critical role in determining the morphology, crystallinity, surface area, and porosity of the resulting nanocomposite.[12,14,15] At the optimized calcination temperature of 550 °C, the rGO–Co_3O_4 nanocomposite exhibits enhanced characteristics, including a well-distributed morphology of Co_3O_4 nanoparticles, improved crystallinity, increased surface area, and controlled porosity. These properties collectively contribute to superior electrochemical performance, with the fabricated microsupercapacitor demonstrating high specific capacitance, excellent rate capability, and improved cycling stability.[25,26]

2.5. Fabrication of flexible microsupercapacitors

The flexible microsupercapacitor was fabricated using a screen-printing technique for the deposition of interdigitated electrodes over the PET substrate (180 microns). The device features an interdigitated electrode structure with precise dimensions: a height of 15.1 mm, a width of 10.4 mm, and a total thickness of 1 mm. Initially, the current collector was printed using commercially available conductive silver ink through three consecutive overprints, each layer being 7 microns thick. The printed layers were dried at 55–60 °C for 30 minutes to ensure uniform adhesion. Subsequently, the electrode material was applied over the silver conductive layer in five successive layers, with each layer measuring 5.6 microns in thickness. This interdigitated pattern is particularly noteworthy as it maximizes the surface area between active electrode material while maintaining a remarkably compact footprint, which is crucial for efficient energy storage at the microscale. This technique was chosen owing to its innate quality to ensure a homogeneous and porous surface during the device printing process. The printing was performed on a flexible substrate, polyethylene terephthalate (PET), using a polyester-based screen mesh with a mesh count of 120 cm (approximately 305 threads per inch, TPI). This mesh was chosen to ensure high-resolution and accurate printing of the interdigitated electrode structures. The screen was prepared with a microsupercapacitor design for imprinting. The printing process was conducted systematically, beginning with the deposition of a commercial silver ink, Loctite ECI-1010-E, followed by the active electrode material in a bottom–up approach. Fig. 1 illustrates this sequence. The dimensions of the resulting flexible microsupercapacitor device were approximately 10.4 × 15.1 mm, with an interdigitated electrode distance of 1 mm.

3. Result and discussions

Fig. 2 reveals XRD patterns of Co_3O_4/rGO nanocomposite, calcined at various annealing temperatures (350 °C, 450 °C, 550 °C, 650 °C, and 750 °C), revealing distinct changes with temperature. At 550 °C, the XRD pattern exhibits characteristic peaks of Co_3O_4 at 18.9° (111), 32.6° (220), 36.8° (311), 44.8° (400), and 59.7° (511), corresponding to the crystallographic planes of Co_3O_4, alongside the broad peak of rGO at 22.3°, suggesting the *d*-spacing of 3.35 Å for (002) plane. This temperature was found to show the best structural characteristics.[27] As the annealing temperature increases to 650 °C and 750 °C, the XRD patterns indicate a noticeable change. The Co_3O_4 peaks shift positively, with slight broadening and reduced intensity, suggesting possible grain growth and changes in crystallinity. At these higher temperatures, the peaks corresponding to Co_3O_4, such as 18.9° (111), 26.4° (002), 32.6° (220), 36.8° (311), 44.8° (400), and

© 2025 The Author(s). Published by the Royal Society of Chemistry

Open Access Article. Published on 10 de març 2025. Downloaded on 17/5/2026 14:58:41.
This article is licensed under a Creative Commons Attribution 3.0 Unported Licence.

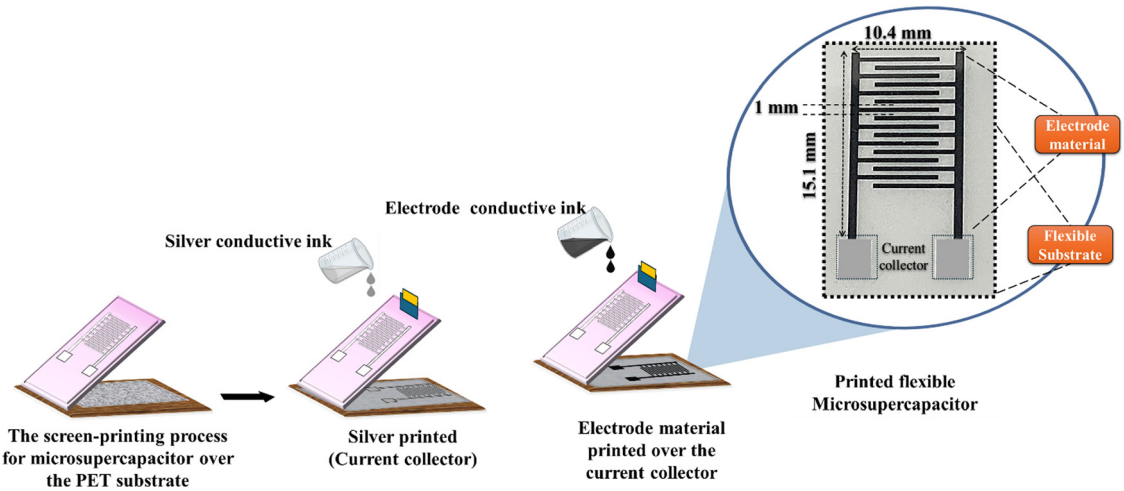

Fig. 1 An illustration of the screen printing and microsupercapacitor fabrication process, along with a dimension representation of the flexible microsupercapacitor.

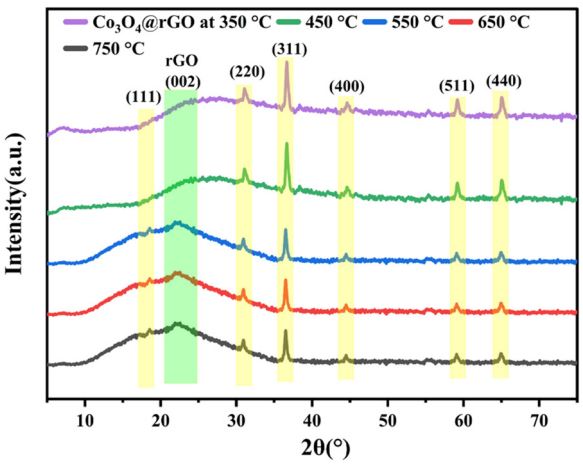

Fig. 2 Illustrates the XRD patterns of Co_3O_4, and rGO nanocomposite namely CR-1, CR-2, CR-3, CR-4 and CR-5.

59.7° (511), show shifts and a decrease in the rGO peak intensity, implying some degradation or reduction in rGO. This trend indicates that while the crystallinity of Co_3O_4 improves with increased temperature, the rGO component experiences structural changes, which may affect the overall properties of the nanocomposite. The optimal temperature for maintaining the desired structural integrity and performance of the Co_3O_4/rGO nanocomposite is thus 550 °C. Debye Scherrer's equation (eqn (S1), ESI†) was used to estimate the average crystallite size of the nanoparticles using equation[28] where D is the crystallite size (nm), K is the Scherrer constant (commonly taken as 0.9 for spherical crystallites), β represents the full width at half maximum (FWHM) of the diffraction peak in radians, λ is the wavelength of the X-ray source (0.1549 nm for Cu Kα radiation), and θ denotes the Bragg diffraction angle in radians. The crystallite size of the CR nanocomposite annealed at 550 °C is calculated to be 22.9 nm using the Scherrer equation. The dislocation density (δ), representing the density of dislocation lines per unit volume, is determined to be 2.87×10^{-3} nm^{-2} using eqn (S2) (ESI†). Furthermore, the average microstrain (ε), which quantifies internal lattice strain, is evaluated as 6.61×10^{-3} based on the XRD peak broadening using eqn (S3) (ESI†).[29] The annealing temperature of 550 °C is identified as optimal for the CR nanocomposite due to its favourable balance of crystallite size, dislocation density, and retention of reduced graphene oxide (rGO) structure, making it particularly suitable for flexible device applications. At 550 °C, the crystallite size of 22.9 nm promotes excellent crystallinity while maintaining a high surface area critical for efficient electrochemical performance. The low dislocation density of 2.87×10^{-3} nm^{-2} indicates a minimal defect density, enhancing the structural stability and mechanical robustness required for flexibility. The microstrain value of 6.61×10^{-3} reflects moderate internal lattice strain, contributing to durability and resilience under mechanical stress, which is essential for the fabrication of flexible devices. Furthermore, the XRD patterns at 550 °C show well-defined peaks for Co_3O_4, while the rGO component remains intact, as evidenced by the broad peak at 22.3°, corresponding to the (002) plane. In contrast, higher annealing temperatures, such as 650 °C and 750 °C, lead to rGO degradation, which significantly reduces its conductivity and compromises the composite's overall performance, including its mechanical flexibility. The nanocomposite annealed at 550 °C, therefore, offers the optimal combination of enhanced crystallinity, low defect density, and intact rGO, ensuring superior electrochemical performance and mechanical flexibility, critical for advanced flexible device applications. Table 1. Shows the crystallite size, dislocation density, and microstrain for CR nanocomposites at different annealing temperatures.

The BET analysis as shown in Fig. S1 (ESI†). reveals a magnificent correlation between calcination temperature (°C) and the prepared electrode material's surface properties, with specific surface area (SSA) (m^2 g^{-1}), total pore volume (cm^3 g^{-1}) at relative pressure of (p/p_0 = 0.4135), and average pore diameter (nm) varying significantly across the prepared samples. At the lower temperature of 350 °C (CR-1), The observed SSA of

Open Access Article. Published on 10 de març 2025. Downloaded on 17/5/2026 14:58:41.
This article is licensed under a Creative Commons Attribution 3.0 Unported Licence.

Table 1 Demonstrates the crystallite size, dislocation density, and microstrain for CR nanocomposites at different annealing temperatures

Temp (°C)	Crystallite size (D)	Average dislocation density (δ)	Average microstrain (ε)
350	~15.5	$\sim 4.17 \times 10^{-3}$	$\sim 8.50 \times 10^{-3}$
450	~18.7	$\sim 2.86 \times 10^{-3}$	$\sim 7.50 \times 10^{-3}$
550	~22.9	$\sim 2.87 \times 10^{-3}$	$\sim 6.61 \times 10^{-3}$
650	~28.5	$\sim 1.23 \times 10^{-3}$	$\sim 5.80 \times 10^{-3}$
750	~35.0	$\sim 0.82 \times 10^{-3}$	$\sim 5.10 \times 10^{-3}$

87.194 $m^2\ g^{-1}$, coupled with a pore volume of 0.00158 $cm^3\ g^{-1}$ and an average pore diameter of 0.6999 nm, suggests that the prepared electrode material retains a relatively dense structure (as evident in the SEM micrograph) with limited porosity. This can be attributed to the onset of thermal activation at this temperature, which facilitates the removal of surface–bound water and weakly adsorbed species without fully decomposing the precursor material. This phenomenon also suggests that 350 °C acts as a transition temperature where initial structural reorganization occurs but does not fully develop the porous network required for higher SSA and pore volume. Thus, rather than partial decomposition, this low SSA and pore volume could be justified as the result of incomplete thermal activation and insufficient energy to generate well-defined pores. By increasing the temperature to 450 °C (CR-2), the SSA improves significantly to 183.1 $m^2\ g^{-1}$ as volatile components (H_2O, CO_x, and NO_x) are removed and replaced by the oxygen (atmospheric O_2),[30] and initial pore development begins. The highest SSA, 614.13 $m^2\ g^{-1}$, is achieved at 550 °C (CR-3), marking this temperature as optimal. This dramatic increase suggests complete removal of organic components and the formation of uniform, thermodynamically stable mesopores that maximize surface area and pore accessibility. However, at higher calcination temperatures (650 °C for CR-4 and 750 °C for CR-5), the SSA sharply declines to 9.367 $m^2\ g^{-1}$ and 5.1337 $m^2\ g^{-1}$, respectively. This reduction can be attributed to sintering effects and the collapse of porous structures, as excessive thermal energy causes particle coalescence and a loss of fine porosity. Furthermore, the total pore volume, peaking at 0.3349 $cm^3\ g^{-1}$ for CR-3 and then dropping drastically at higher temperatures due to pore collapse. Interestingly, the average pore diameter remains relatively stable across all samples, with a minor reduction for CR-3 (0.7648 nm), indicative of smaller, well-defined pores contributing to its high surface area and pore volume. In contrast, the slight increase in pore diameter for CR-4 and CR-5 suggests pore merging and structural degradation. These results establish 550 °C as the optimal calcination temperature, balancing pore formation and structural integrity, while higher temperatures lead to diminished textural properties due to thermal damage.[31,32] Table S1 (ESI†) shows the detailed tabulated data for SSA and various other parameters under the influence of temperature. Scanning electron microscopy (SEM) was conducted to analyse the size and morphology of pristine ZIF and Co_3O_4 annealed at various temperatures, identified as CR-1, CR-2, CR-3, CR-4, and CR-5. In Fig. 3(a), the pristine ZIF nanoparticles exhibit a well-defined cubic shape, uniformly distributed across a smooth surface, indicating a high level of structural integrity before annealing. The cubic morphology is a characteristic feature of ZIF-67. Upon annealing at 350 °C, as shown in Fig. 3(b), the ZIF-67 precursor transforms into porous Co_3O_4 nanoparticles, which take the form of nanospheres. These nanospheres display a notable porous structure, indicative of the thermal decomposition of the ZIF-67 framework, resulting in the formation of Co_3O_4 with substantial surface area, which is critical for electrochemical applications. As the annealing temperature increases to 450 °C, shown in Fig. 3(c), the Co_3O_4 nanoparticles retain their spherical morphology, but with more developed and well-defined porosity compared to the sample annealed at 350 °C. The higher temperature further enhances the pore structure, allowing for increased surface area and potentially improved electrochemical performance. The porous nature is highlighted by the coloured encircling around graphitic sheets throughout the SEM images, emphasizing the importance of these pores in contributing to the material's overall functionality. At 550 °C, the morphology of Co_3O_4/rGO, illustrated in Fig. 3(d), reaches an optimal state, with the nanospheres demonstrating well-maintained porosity and a uniform distribution of pores. The Co_3O_4 nanoparticles exhibit an enhanced interaction with the reduced graphene oxide (rGO) sheets, creating a highly interconnected network that is ideal for applications such as energy storage. This annealing temperature produces the most favourable structure, with a balanced combination of porosity and particle stability. However, when the annealing temperature is increased to 650 °C, the Co_3O_4 nanoparticles start to display signs of agglomeration as shown in Fig. 3(e). The once distinct nanospheres begin to merge, and the pore uniformity decreases, as the particles start to lose their separation. Although the pore structure is still present, it becomes less ordered, and the interconnected nature of the particles indicates the early stages of structural degradation. At 750 °C, Fig. 3(f) shows the morphology of the Co_3O_4 nanoparticles undergoes significant changes. The particles lose their well-defined spherical shape and become irregular and clumped together, signifying extensive particle fusion. The pore structure, though still visible, is greatly reduced due to the merging of the nanoparticles, leading to a significant decrease in surface area. This fusion and agglomeration result in a less favourable structure for applications requiring high porosity and surface area, such as microsupercapacitors. Additionally, the cubic structure of the ZIF precursor is lost at temperatures above 550 °C, likely due to the intense etching of the ZIF-67 framework, caused by the enhanced release of oxygen species from the reduced graphene oxide (GO). This structural change further contributes to the degradation of the material's electrochemical properties at higher temperatures.

The elemental distribution and composition of the Co_3O_4/rGO-based nanocomposite were analysed using energy dispersive X-ray (EDX) mapping, as shown in Fig. 3(g)–(l). The SEM image of the CR-1 sample at 5 μm magnification provides a detailed visual of the nanocomposite, illustrating the spatial distribution of essential elements including carbon (C), cobalt

© 2025 The Author(s). Published by the Royal Society of Chemistry

Open Access Article. Published on 10 de març 2025. Downloaded on 17/5/2026 14:58:41.
This article is licensed under a Creative Commons Attribution 3.0 Unported Licence.

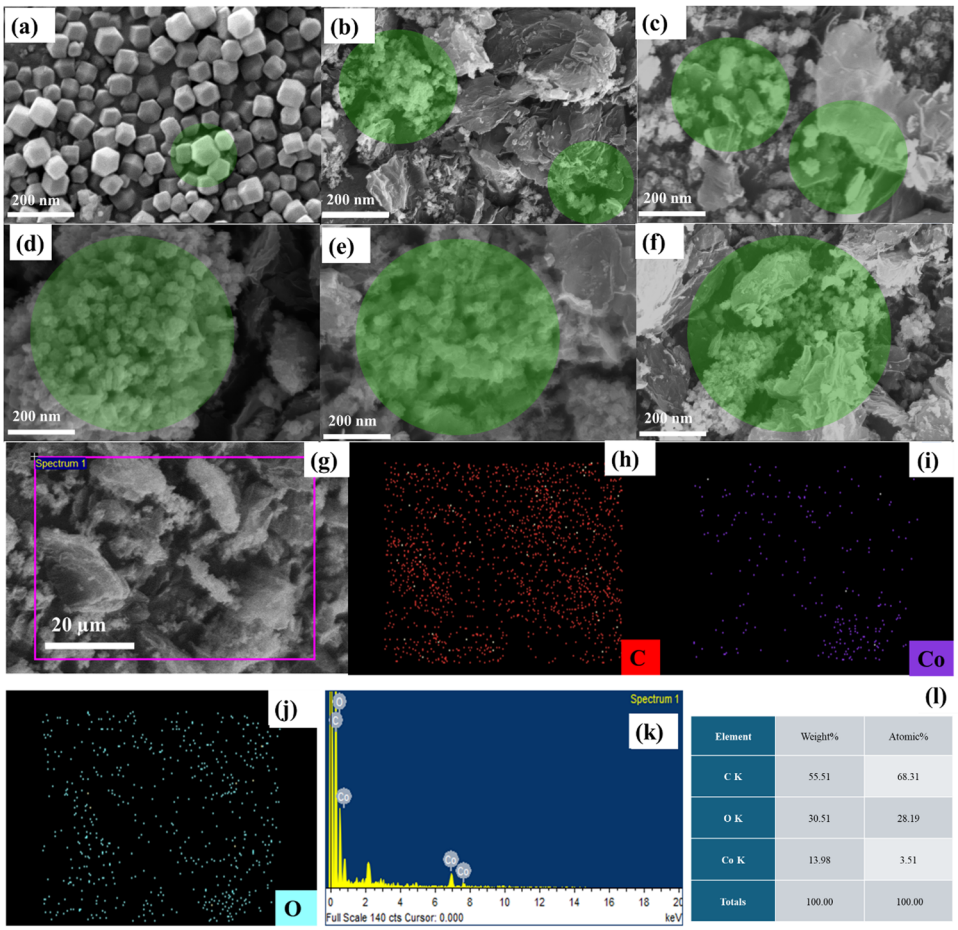

Fig. 3 SEM images showing (a) pristine Co_3O_4, (b) CR-1 calcined at 350 °C, (c) CR-2 calcined at 450 °C, (d) CR-3 calcined at 550 °C, (e) CR-4 calcined at 650 °C, and (f) CR-5 calcined at 750 °C. (g) EDX spectrum displaying the elemental composition of the nanocomposites. The elemental mapping shows the distribution of (h) carbon, (i) cobalt, and (j) oxygen, along with the combined elemental representation in spectra (k) and tabulated (l).

(Co), and oxygen (O). EDX mapping allows for precise identification and visualization of these elements, with distinct colours representing each element and the intensity reflecting their relative concentrations within the sample. The EDX mapping of the Co_3O_4/rGO composite shows a uniform distribution of Co_3O_4 nanoparticles across the reduced graphene oxide matrix, ensuring effective incorporation of Co_3O_4 within the layered structure. This uniform dispersion is vital for optimizing the resultant electrochemical output for flexible microsupercapacitor, as proven by the EDX analysis. XPS was used to measure the binding energies of the elements as shown in Fig. 4(a)–(d) to confirm their chemical states and determine the surface chemical composition. The survey spectra of ZIF-derived CR-5 show the existence of elements (cobalt, carbon, and oxygen). The deconvoluted C 1s spectra shown in Fig. 4(a) illustrate a primary peak at 284.56 eV corresponding to the C (sp^2) C–C bond, with additional peaks at 285.46 eV and 288.46 eV attributed to oxygen active groups, specifically (C–O) and (COO-R), respectively. The C 1s peak is broader at lower temperatures and becomes narrower in electrode material treated at higher temperatures. This suggests an improved structural organization within the carbon framework. Furthermore, it indicates C 1s peak diminishes and decreases with increasing temperature, corresponding to a reduction in oxygen functional groups. Fig. 4(c) The deconvoluted high-resolution O 1s spectra show peaks at 529.96, 531.36, and 533.26 eV, corresponding to (O–Co), $Co(OH)_2$, carbonyl groups (C═O), and oxygen bonded to carbon in phenolic groups (O–C), respectively. Notably, the peaks associated with cobalt–oxygen bonding (O–Co) and carbon–oxygen bonding (O–C) provide further insights. The high-resolution Co 2p spectra in Fig. 4(d) reveal two primary peaks at 780.26 and 795.46 eV, corresponding to Co $2p_{3/2}$ and Co $2p_{1/2}$, with an energy separation of 15.2 eV. Upon further deconvolution, four peaks appear at 779.9 eV (Co $2p_{3/2}$), 781.4 eV (Co $2p_{3/2}$), 794.9 eV (Co $2p_{1/2}$), and 796.6 eV (Co $2p_{1/2}$), representing the two spin doublets characteristic of the Co 2p spectrum. The peaks near 779.4 eV and 794.3 eV indicate the presence of octahedral Co^{3+} in Co_3O_4, while those around 781.3 eV and 796.2 eV suggest the tetrahedral Co^{2+} oxidation state. Moreover, shake-up satellite peaks characteristic of the Co_3O_4 phase are observed.

Fig. S2 (ESI†) presents the atomic force microscopy (AFM) analysis conducted to examine the surface morphology of the screen-printed microsupercapacitor device on a PET substrate.

Open Access Article. Published on 10 de març 2025. Downloaded on 17/5/2026 14:58:41.
This article is licensed under a Creative Commons Attribution 3.0 Unported Licence.

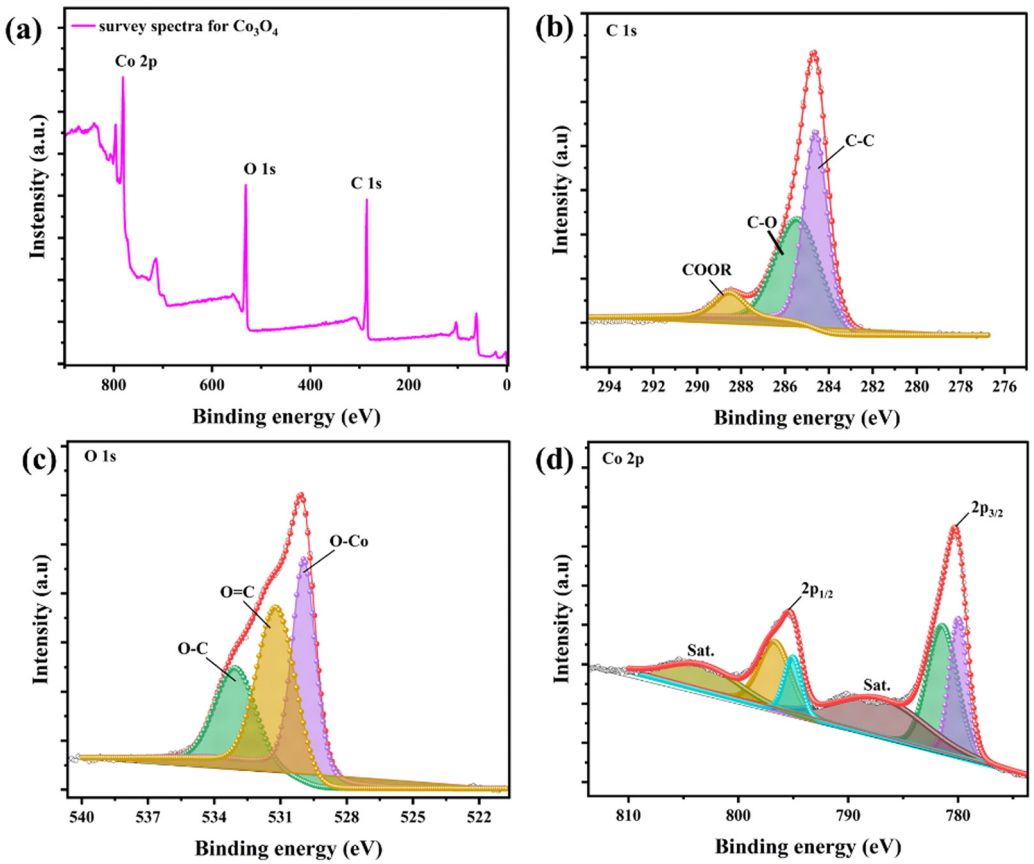

Fig. 4 Deconvoluted XPS spectra of (a) a wide scan spectrum (b) the C 1s peak (c) the O peak and (d) the Cobalt 2p peak for CR-3.

One of the key quantitative parameters obtained from AFM height images is surface roughness, which is crucial for evaluating the morphological characteristics of the material's surface. The root mean square (RMS) roughness is a widely used metric in AFM analysis to quantify surface roughness. Surface roughness plays an essential role not only in determining the physical texture of the material but also in influencing its functional properties, such as adhesion, conductivity, and mechanical behaviour. Variations in roughness values often provide valuable insights into molecular properties and structural changes, which may occur due to environmental conditions or fabrication techniques. In this case, the AFM topographic image of the screen-printed Co_3O_4/rGO composite shows an RMS roughness value (σ_{rms}) of 77.13 nm, indicating a relatively uniform surface. This degree of roughness could impact the adhesion between the nanocomposite and the flexible PET substrate, ultimately influencing the overall performance of the device, particularly in energy storage applications.

Viscosity is a crucial factor in the formulation and functionality of conductive inks, especially for screen printing applications. Achieving the right viscosity balance is essential as the ink must be fluid enough to pass smoothly through the screen mesh under the pressure applied by the squeegee, yet sufficiently viscous to maintain the integrity of the printed design, avoiding distortion or spreading. Temperature significantly affects the viscosity of conductive inks. As the temperature rises, viscosity typically decreases due to the reduction of intermolecular forces and the increased mobility of ink particles or polymer chains. This temperature–viscosity relationship is well-established in the literature,[33] where the decline in viscosity with increasing temperature is attributed to the loosening of molecular interactions within the ink. For CR nanocomposite-based conductive inks, viscosity measurements performed at 25 °C, 35 °C, and 45 °C using an advanced modular rheometer demonstrated a distinct non-Newtonian, shear-thinning behaviour, as illustrated in Fig. 5(a). The calculated viscosity of the formulated ink decreases significantly with an increase in temperature from 25 °C to 45 °C. At 25 °C, the viscosity is measured as η = 6879.3 mPa s, which decreases to η = 3319.7 mPa s at 35 °C and further to η = 2277.4 mPa s at 45 °C, over a varying shear rate range of 0 to 700 s^{-1}, as depicted in Fig. 5(a). To gain deeper insights into the rheological behaviour of the ink, the shear stress (Pa) was also analysed as shown in Fig. 5(b). The relationship between shear stress and shear rate provides valuable information about the ink's flow properties, ensuring its suitability for screen-printing applications. These analyses help in optimizing the ink composition to achieve the desired balance between viscosity and flowability, which is crucial for precise deposition on substrates. Proper flowability prevents clogging of the screen mesh and ensures consistency in spreading over the PET substrate. The ink exhibits shear-thinning behaviour, also known as pseudoplasticity, where the viscosity decreases with increasing shear rate. This characteristic is particularly advantageous in screen printing, as the ink flows easily under applied

© 2025 The Author(s). Published by the Royal Society of Chemistry

Open Access Article. Published on 10 de març 2025. Downloaded on 17/5/2026 14:58:41.
This article is licensed under a Creative Commons Attribution 3.0 Unported Licence.

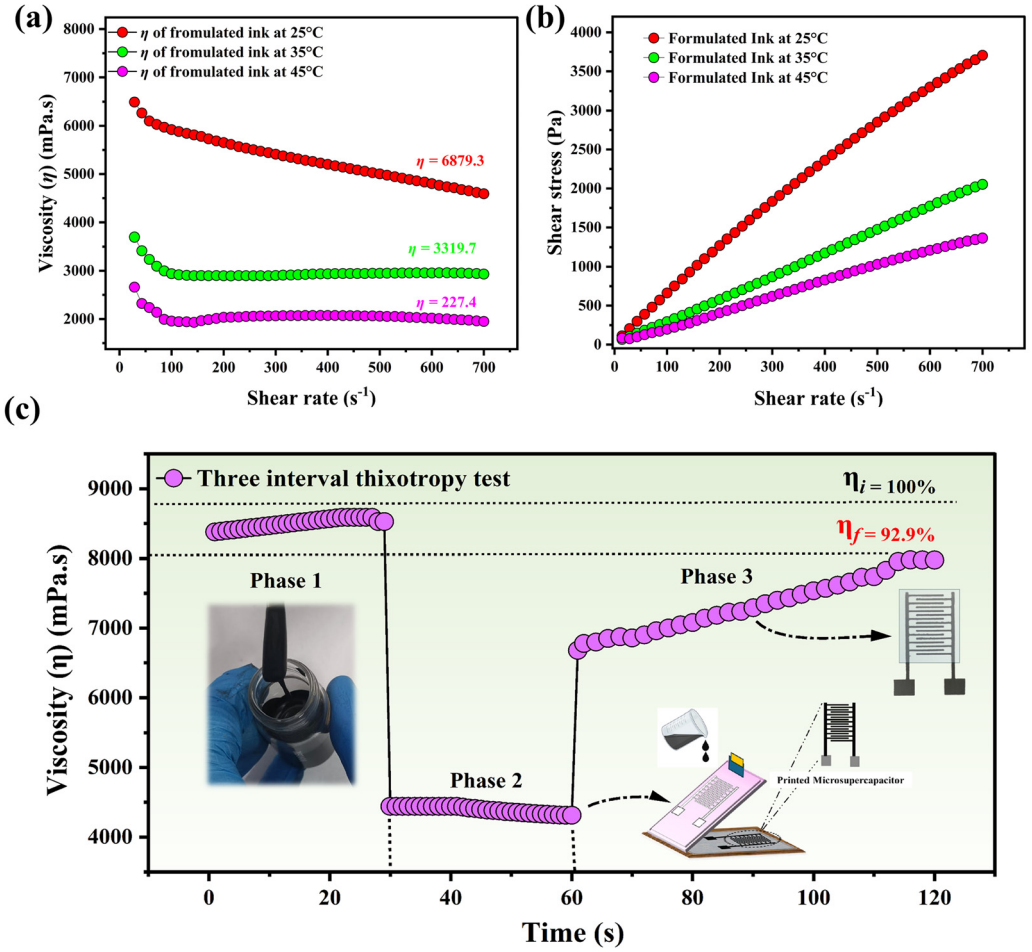

Fig. 5 Viscosity analysis at various from 25 °C to 45 °C (a) shear stress analysis at various (b) the C 1s peak (c) 3ITT for the time-dependent viscosity analysis.

shear force during the printing process but regains its viscosity once the shear force is removed. This recovery ensures the printed pattern maintains high resolution without spreading inconsistencies. The non-Newtonian nature of the Co_3O_4/rGO ink is attributed to the complex interactions between the Co_3O_4 nanoparticles and rGO sheets dispersed within the ink. These particles form a network-like structure that dictates the rheological properties. Under applied shear stress, this network temporarily breaks down, reducing the viscosity and allowing smooth flow through the screen. Upon removal of the shear force, the network structure reforms, restoring the ink's viscosity, thereby retaining the sharpness of the printed features and preventing unwanted spreading. To further investigate the time-dependent viscosity changes during the printing process, a three-interval thixotropy test (3iTT) was conducted. This test is designed to simulate the different stages of ink behaviour during screen printing. In the first phase, the ink undergoes homogenization under low shear stress, ensuring a uniform distribution of its components. The second phase involves the application of high shear stress, mimicking the stroking action of the squeegee during the screen-printing process, where the ink's viscosity decreases to facilitate smooth flow through the screen. In the final phase, known as the low-shear recovery phase, the ink regains its viscosity after the removal of shear stress, which is critical for maintaining the resolution and sharpness of the printed features.[9] The recovery ratio of the ink, indicating the extent to which the ink regains its initial viscosity after the shear stress is removed, was calculated using eqn (1).

$$\text{Recovery ratio} = \frac{\text{Viscosity after time } (t)\eta_f}{\text{Initial viscosity } \eta_i} \times 100 \quad (1)$$

here, η_i is the initial viscosity, and η_f is the final viscosity after the recovery phase. For the formulated ink, η_i = 8529.4 mPa s^{-1} and η_f = 7977.4 mPa s^{-1}, resulting in a recovery ratio of 92.2%. This indicates the ink's excellent thixotropic properties, ensuring efficient recovery and stability during the screen-printing process for flexible microsupercapacitor fabrication. Incomplete recovery or too rapid recovery can lead to surface defects or poor electrical connectivity, ultimately impacting the overall device efficiency and reliability. The structure and uniformity of the interdigitated electrodes are closely correlated with the rheological properties of the formulated CR's nanocomposite ink, including viscosity, shear-thinning behaviour, and shear recovery characteristics. These properties are crucial in ensuring precise deposition and maintaining the resolution of the printed interdigitated patterns during the

Open Access Article. Published on 10 de març 2025. Downloaded on 17/5/2026 14:58:41.
This article is licensed under a Creative Commons Attribution 3.0 Unported Licence.

screen-printing process. The consistent viscosity of the ink (η = 6879.3 mPa s at room temperature) allows it to flow uniformly through a screen mesh with 120 cm counts, preventing irregularities in layer thickness that could result in uneven current distribution and increased resistive losses.[34,35] The shear-thinning behaviour ensures that the ink flows readily under applied shear stress, enabling the formation of interdigitated patterns with sharp edges and minimal spreading over the flexible PET substrate. Upon the removal of shear force, the ink exhibits rapid recovery of viscosity (η = 7977.4 mPa s), effectively preventing spreading beyond the intended boundaries and preserving the Precision of the electrode interdigitated fingers. A uniform and well-defined interdigitated structure not only increases the effective surface area of the electrodes, improving ionic accessibility but also guarantees optimal charge storage and transfer. This intricate interplay between the rheological properties of the ink and the structural integrity of the electrodes significantly enhances the electrochemical performance, leading to higher areal capacitance, superior charge–discharge stability, and overall improved functionality of the microsupercapacitors. To further explore the interactions between Co_3O_4/rGO conductive ink and PET substrates, we utilized an Ossila goniometer to measure both the contact angle and surface tension of the formulated ink. These parameters are critical for understanding the ink's wettability, spreading behavior, and overall performance in printing applications. In our study, Fig. S3(a)–(c) illustrates the contact angle measurements, recorded at specific intervals, revealing a progressive decrease over time. Initially, the contact angle was approximately 55.54° at 71 s, decreasing to 54.13° at 81 s, and further to 53.19° at 91 s. This trend indicates an improvement in the ink's wettability on the PET substrate, suggesting that the Co_3O_4/rGO conductive ink exhibits enhanced spreading and adhesion characteristics. Simultaneously, Fig. S3(d)–(f) (ESI†) presents the surface tension measurements, used to assess the spreading and adhesion characteristics of the conductive ink. The recorded surface tension values were 1354.1 mN m^{-1} at 71 s, 907.7 mN m^{-1} at 81 s, 846.4 mN m^{-1} at 91 s, and 514.3 mN m^{-1} at 100 s. The observed decrease in surface tension over time further supports the improved wettability of the ink, indicating that it interacts more effectively with the PET substrate as time progresses. Together, these measurements underscore the importance of both contact angle and surface tension in determining the suitability of the CR-based nanocomposite conductive ink for screen printing applications. Improved wettability, as evidenced by the decreasing contact angle and surface tension, facilitates better ink distribution and bonding with the substrate, which is essential for optimizing the functionality and reliability of printed devices.

4. Electrochemical evaluation

The electrochemical evaluation of the CR-based nanocomposite was thoroughly evaluated using an all-printed micro-supercapacitor, in a two-electrode configuration with a 1 M KOH electrolyte. To investigate the electrochemical behaviour, cyclic voltammetry (CV) was conducted with a potential range of 0 to 1.0 V, utilizing scan rates between 5 to 100 mV s^{-1} for both symmetric and asymmetric device setups. The CV curves provided insights into the charge storage mechanisms, indicating both capacitive and faradaic contributions to the overall performance. Electrochemical impedance spectroscopy (EIS) was performed over a broad frequency range from 1 MHz to 100 mHz, to analyse the impedance characteristics of the nanocomposite. This test was critical for understanding the internal resistance, charge transfer processes, and diffusion limitations of the electrodes. The resulting Nyquist plots revealed information about the charge transfer resistance (R_{ct}) and the overall device conductivity, shedding light on the ion diffusion within the electrolyte and the nanocomposite structure. Furthermore, galvanostatic charge/discharge (GCD) tests were conducted at room temperature over a voltage range of 0 to 1 V. These tests, carried out using the Biologic SP50e system, provided valuable data on the charge/discharge times, the specific capacitance, energy density, and power density of the CR-based microsupercapacitors. The symmetric devices showed stable charge/discharge profiles with minimal voltage drop, while the asymmetric devices demonstrated improved energy storage capabilities due to the complementary electrochemical characteristics of the two electrode materials. The combination of CV, EIS, and GCD analyses highlighted the superior electrochemical properties of the CR-based nanocomposites, particularly at the optimized annealing temperature, which provided a balance between conductivity, ion diffusion, and overall charge storage efficiency.

To further explore the resistance properties of the Co_3O_4-based electrode materials, electrochemical impedance spectroscopy (EIS) measurements were carried out over a frequency range of 1 MHz to 100 mHz. EIS is a vital tool for evaluating the electrical performance of supercapacitor electrodes as it provides detailed insights into various resistive and capacitive elements present in the system. Since supercapacitors are typically designed for power delivery, minimizing the internal resistance of electrode materials is crucial for optimizing their electrochemical performance. In this study, the impedance characteristics of the Co_3O_4 electrode were analysed through Nyquist plots, which were generated from the EIS data. Nyquist plots provide a complex-plane representation of impedance, displaying the real part (Z') on the x-axis and the imaginary part (Z'') on the y-axis. These plots are instrumental in illustrating key parameters such as solution resistance (R_s) and charge transfer resistance (R_{ct}), both of which are critical for understanding the electrochemical behaviour of the system. The solution resistance (R_s), which corresponds to the intercept of the Nyquist curve with the real axis at high frequencies, represents the resistance of the electrolyte and the inherent resistance of the device components. The lowest R_s value, approximately 5 Ω, was observed for the electrode material annealed at 550 °C, indicating improved ionic conductivity. Conversely, the highest R_s of around 10 Ω was found in the material annealed at 750 °C, suggesting greater resistance to ion transport in the system. The charge transfer resistance (R_{ct}), which is reflected by the diameter of the semicircular region in

© 2025 The Author(s). Published by the Royal Society of Chemistry

Open Access Article. Published on 10 de març 2025. Downloaded on 17/5/2026 14:58:41.
This article is licensed under a Creative Commons Attribution 3.0 Unported Licence.

the Nyquist plot at mid-high frequencies, provides insight into the charge transfer kinetics at the electrode/electrolyte interface. The material annealed at 550 °C exhibited the lowest R_{ct} value of 45 Ω, highlighting efficient charge transfer and enhanced electrochemical performance as shown in Fig. 6(a). In contrast, the material annealed at 350 °C exhibited a significantly higher charge transfer resistance (R_{ct}) of 90 Ω, indicating less efficient charge transfer and reduced device performance. Higher R_{ct} values are indicative of slower charge transfer kinetics at the electrode–electrolyte interface, which

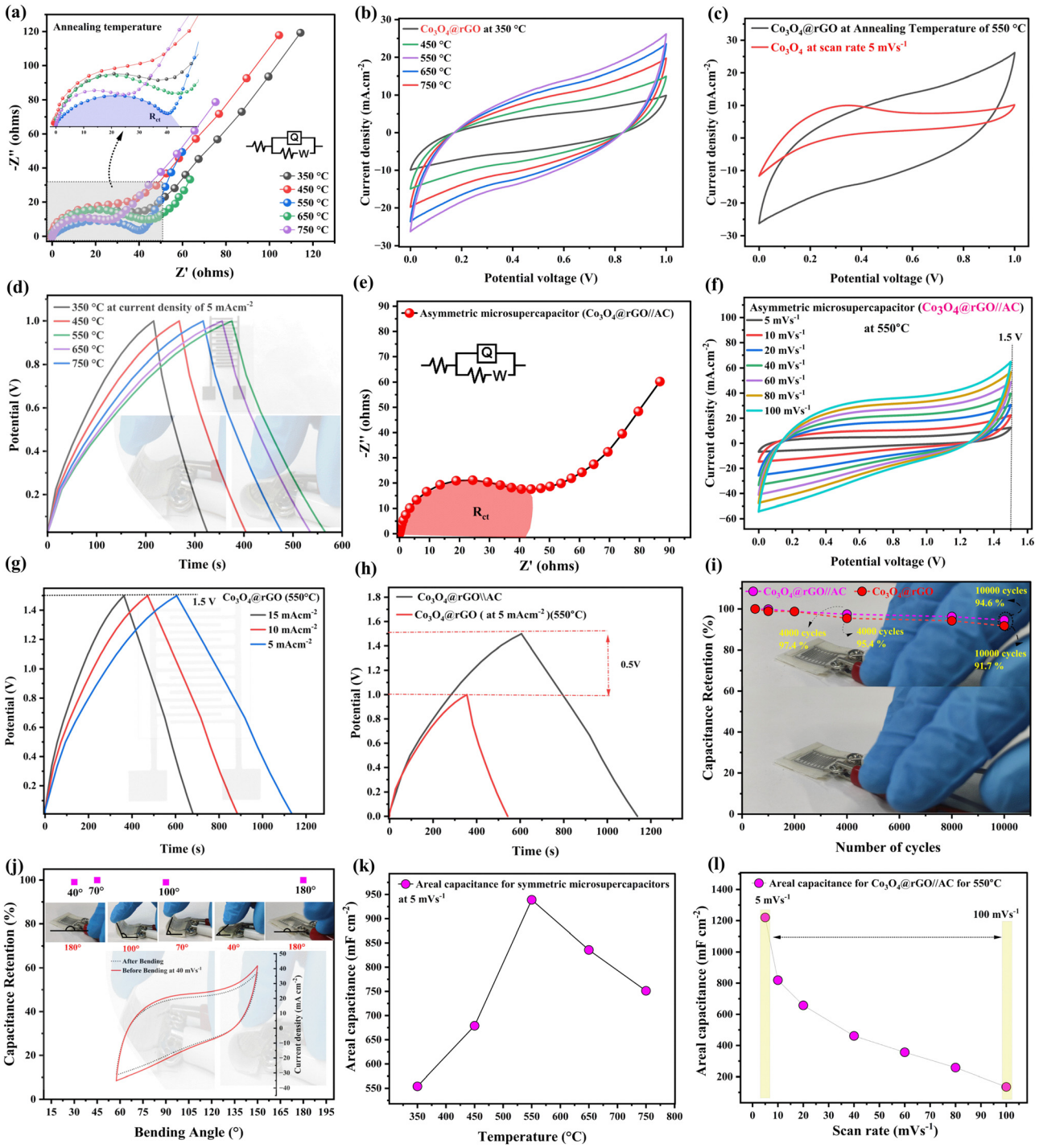

Fig. 6 (a) Impedance analysis for CR-1 to CR-5 at different annealing temperatures. (b) CV performance of CR-1 to CR-5 at 5 mV s^{-1}. (c) Comparison of pristine Co_3O_4 and Co_3O_4/rGO at 550 °C. (d) GCD analysis, (e) EIS of the asymmetric device, (f) CV of the asymmetric device at 550 °C, (g) GCD of the asymmetric device, (h) comparative analysis for GCD. (i) Show the capacitance retention over various cycles, (j) flexibility curve of the device, (k) shows the areal capacitance for the symmetric microsupercapacitor at 5 mV s^{-1}, and (l) shows the areal capacitance for the asymmetric microsupercapacitor for various scan rate.

Open Access Article. Published on 10 de març 2025. Downloaded on 17/5/2026 14:58:41.
This article is licensed under a Creative Commons Attribution 3.0 Unported Licence.

hampers the overall electrochemical activity. On the other hand, lower R_s and R_{ct} values correspond to improved ionic and electronic conductivity, enhancing both the capacitive behaviour and energy storage capabilities of the supercapacitor. Among the annealing temperatures tested, the 550 °C condition demonstrated the most favourable electrochemical performance, as reflected by its lower resistance values. Specifically, the R_{ct} of 45 Ω and R_s of 5 Ω indicate superior charge transfer and minimal solution resistance, respectively as shown in Fig. 6(e). This combination contributes to enhanced capacitive behaviour and optimized energy storage performance. Table S2 (ESI†) provides tabulated impedance data R_s and R_{ct}, highlighting that the electrode annealed at 550 °C shows the best performance due to its low resistance values, leading to improved ionic/electronic conductivity and enhanced energy storage capabilities. In the present study, we conducted a detailed cyclic voltammetry (CV) study to investigate the influence of calcination temperature on the electrochemical performance of CR-based electrodes, synthesized by calcining ZIF-67 and graphene oxide (GO) at various temperatures (350 °C, 450 °C, 550 °C, 650 °C, and 750 °C). The primary objective was to determine the optimal calcination temperature for maximizing the areal capacitance of the Co_3O_4@rGO electrode material. Fig. 6(c) shows The CV voltammogram compares the pristine Co_3O_4 electrode with the Co_3O_4@rGO composite annealed at 550 °C. The CV measurements were performed within a potential window of 1 V at a scan rate of 5 mV s^{-1}. The electrodes exhibited typical redox peaks associated with the faradaic processes of Co_3O_4, indicating the successful integration of Co_3O_4 onto the rGO matrix. Among the various temperatures, the electrode material calcined at 550 °C demonstrated superior electrochemical performance, as attested by the significantly larger enclosed CV area, corresponding to a higher areal capacitance. The superior performance of the Co_3O_4@rGO electrode calcined at 550 °C can be attributed to an optimal balance between the crystallinity of Co_3O_4 and the structural integrity of the rGO Fig. 6(f). At this temperature, the calcination process facilitates the formation of well-crystallized Co_3O_4 nanoparticles uniformly distributed on the rGO surface, enhancing the electroactive surface area and the efficiency of ion transport within the electrode. In contrast, electrodes calcined at temperatures lower than 550 °C may not achieve the necessary crystallinity, while those treated at higher temperatures could suffer from excessive growth of Co_3O_4 particles, leading to reduced surface area and compromised electrochemical activity. This study underscores the critical role of calcination temperature in tailoring the electrochemical properties of Co_3O_4@rGO electrodes, with the 550 °C calcined sample exhibiting the highest areal capacitance, making it an appealing prospect for applications necessitating high-performance energy storage. To investigate the practical aspect of an energy storage device, a microsupercapacitor asymmetric device was fabricated using screen printing with activated carbon serving as the counter electrode and CR-5 as the working electrode. The CV of the ASSC demonstrated a characteristic electric double-layer capacitor (EDLC) behaviour, with a near-rectangular shape and minimal deviation within the 0–1.5 V range. This outcome highlights the superior specific capacitance of the flexible device. The inclusion of carbon material significantly influenced the voltammograms, which are emblematic of EDLC-type energy storage, thereby confirming the device's robust energy storage performance. The areal capacitances of the device were quantitatively evaluated using eqn (2), providing an accurate assessment of its capacitance performance.

$$C_A = \frac{\int I \, dv}{VS\Delta V} \quad (2)$$

Eqn (2) was employed to calculate the areal capacitance of the microsupercapacitor. The equation incorporates parameters including $\int I \, dv$, representing the integrated area under the CV curve, 'V' denoting the scan rate (V s^{-1}), S represent active area of the electrode and 'ΔV' specifying the applied voltage window (0–1 V).

Galvanostatic charge–discharge (GCD) testing was performed at current densities ranging from 5 to 15 mA cm^{-2}, within a voltage window of 0 to 1.5 V, to quantitatively assess the electrochemical performance. The GCD analysis was performed to study the correlation between the annealing temperature and the electrochemical performance for the Co_3O_4/rGO electrodes materials were annealed at temperatures ranging from 350 °C to 750 °C, with 550 °C emerging as the optimal temperature for achieving superior electrochemical characteristics. The GCD analysis of this electrode material revealed superior electrochemical performance, showcasing a combination of high specific capacitance and excellent cycling stability (94.6%). The electrode material annealed at 550 °C demonstrated a balance between crystallinity and porosity, contributing to its enhanced charge storage capabilities. Upon comparison of all the electrode materials, an elevation in the pyrolysis temperature was observed to boost the efficiency, as illustrated for the fabricated asymmetric microsupercapacitor in Fig. 6(g). This discerned trend can be attributed to the low efficiency coupled with the rapidly degrading discharge profiles at low temperatures. This highlights the electrode material's incapability to charge electrochemically, possibly due to the limited electronic conductivity and surface area. The internal resistance (IR) of microsupercapacitors is emphasized, as the IR drop is challenging to detect due to the rapid degradation of discharge profiles for materials annealed at lower temperatures. However, the overall performance remains lower than other materials, suggesting that limited porosity may also contribute to this limitation. Lower annealing temperatures (350 °C and 450 °C) produced less crystalline structures, leading to reduced electrochemical performance, while higher annealing temperatures (650 °C and 750 °C) caused excessive crystallite growth and potential aggregation, reducing the electrode's surface area and performance. The areal capacitance (C_g) is calculated using eqn (3). Additionally, the energy density and power density of the device were determined using eqn (4) and (5).

$$C_g = \frac{I\Delta t}{S\Delta V} \quad (3)$$

© 2025 The Author(s). Published by the Royal Society of Chemistry

Open Access Article. Published on 10 de març 2025. Downloaded on 17/5/2026 14:58:41.
This article is licensed under a Creative Commons Attribution 3.0 Unported Licence.

$$E_D = \frac{C_A \times (\Delta V)^2}{7.2} \quad (4)$$

$$P_D = 3.6 \times \frac{E_A}{\Delta t} \quad (5)$$

Eqn (3) is utilized to evaluate the capacitance (C_g) mF cm^{-2}, where 'I' denotes the current density employed for charge and discharge, ΔV represents the potential voltage (V), S' represents the area of the fabricated microsupercapacitor (1.5 cm^2) and Δt indicates the period of discharge. To explore the practical application potential of Co_3O_4/rGO in microsupercapacitors, an asymmetric device (Co_3O_4/rGO//AC) was fabricated using 1 M KOH as the electrolyte, with Co_3O_4/rGO as the positive electrode and activated carbon (AC) as the negative electrode. Fig. 6(f) shows the CV curves of the best-performing device annealed at 550 °C, tested in an as-assembled asymmetric supercapacitor at various scan rates ranging from 5 to 100 mV s^{-1}. As anticipated, the working voltage of the asymmetric microsupercapacitors can be incremented to 1.5 V, by completely leveraging the different potential windows of the Co_3O_4/rGO heterostructure and activated carbon, demonstrating the capability of the integrated system in real-world applications. The GCD curves of the asymmetric supercapacitor are shown in Fig. 6(g). An improved areal capacitance of 1220.2 mF cm^{-2} can be achieved at 5 mA cm^{-2} for the asymmetric microsupercapacitor. The electrode material Co_3O_4/rGO//AC asymmetric supercapacitor can yield a superior energy density of 343.51 μW h cm^{-2}, and a extremely high power density of 3876.6 mW cm^{-2}. The Fig. 6(i) shows the capacitance retention for the fabricated microsupercapacitor over 10 000 cycles. The asymmetric microsupercapacitor (ASSC) demonstrated excellent long-term stability, exhibiting remarkable capacitance retention over extended cycling. After 4000 cycles, the ASSC retained 97.4% of its initial capacitance. Even after 10 000 cycles, the supercapacitor maintained a high capacitance retention of 94.6%, highlighting its durability and stable electrochemical performance. The microsupercapacitor was subjected to bending at various angles of 40°, 70°, and 100°, during which it exhibited minimal distortion, indicating excellent mechanical flexibility and structural integrity under mechanical stress as demonstrated in Fig. 6(j). This demonstrates its suitability for applications in flexible and wearable electronic devices. The areal capacitance for the symmetric and asymmetric microsupercapacitor as shown in Fig. 6(k)–(l) furthermore, the effect of overprints (OPs) on the fabricated asymmetric microsupercapacitors, which use electrode material deposition by screen-printing techniques, is analysed at various overprints of 3, 5, 7, and 9 OPs, as shown in Fig. S4 (ESI†), with a layered thickness of approximately 5.6 microns. As the layered thickness increases from 3 OPs to 9 OPs, there is a gradual increase in the areal capacitance (418 mF cm^{-2} to 507 mF cm^{-2}) as shown on Fig. S4(c) (ESI†). However, at 9 Ops and beyond, the resolution starts to degrade, leading to a reduction in the overall structural integrity fabricated microfabricated and electrochemical performance of the electrode material.

In the investigation of energy storage mechanisms, both diffusion and capacitive processes play crucial roles. Their individual contributions were assessed by analysing cyclic voltammetry (CV) curves recorded at various scan rates. The detailed analysis of these storage behaviours was carried out using eqn (6).

$$i = av^b \quad (6)$$

The constants a and b were evaluated to characterize the storage behaviour, with the b value indicating the nature of the charge storage mechanism. A b value of 0.5 suggests diffusion-controlled processes, while a value of 1.0 indicates capacitive processes. The b values were derived from the cathodic and anodic currents in the CV curves by plotting the logarithm of the scan rates against the logarithm of the current, as shown in Fig. 7(a). The specific contributions of diffusion-controlled and capacitive processes were further quantified using the corresponding eqn (7).

$$\frac{i}{v^{0.5}} = k_1 v^{0.5} + k_2 \quad (7)$$

In this study, the term k_1v represents the capacitive contribution, while $k_2v^{0.5}$ corresponds to the diffusion-controlled process. A plot of the square root of the scan rate *versus* $i(v)/v^{0.5}$ delineated the distinct capacitive and diffusion behaviours of the electrode material, as indicated by the linear trend shown in Fig. 7(b). The incorporation of reduced graphene oxide (rGO) into the Co_3O_4 matrix is expected to enhance capacitive performance due to the formation of an electrical double-layer capacitance (EDLC) at the electrode–electrolyte interface. Both electrode materials demonstrated an R^2 value close to 1, suggesting a high degree of accuracy in the measurements, as illustrated in Fig. 7(c). The contributions from diffusion and capacitive processes to the total charge storage at various scan rates are presented in Fig. 7(d). The capacitive contribution was found to increase progressively, accounting for approximately 43%, 45%, 51%, 60%, 64%, 69%, and 76% of the total charge storage at scan rates ranging from 5 to 100 mV s^{-1}, respectively. As the scan rate increases, the capacitive contribution becomes more dominant, while the diffusion-controlled contribution decreases. This behaviour could be due to the higher scan rates which potentially enable faster interaction between the electrolyte ions and the electrode surface, thereby reducing the time available for diffusion processes to occur.[36,37]

5. Full factorial DoE for statistical modeling

A two-level, two-parameter full factorial DoE was run to obtain the model equations correlating the output parameters with the input parameters as shown in Table S3 (ESI†). The number of CV cycles was taken as an input parameter just to satisfy the minimum criteria for carrying out optimal custom modeling in RSM but was kept constant to comprehend the temperature's exclusive effect on the output characteristics. While studying the relationship of temperature with the response variables, DoE ensures to maintain a minimum number of experimental trials and provides an optimized experimental matrix. This matrix not only considers the strategically chosen data points

Open Access Article. Published on 10 de març 2025. Downloaded on 17/5/2026 14:58:41.
This article is licensed under a Creative Commons Attribution 3.0 Unported Licence.

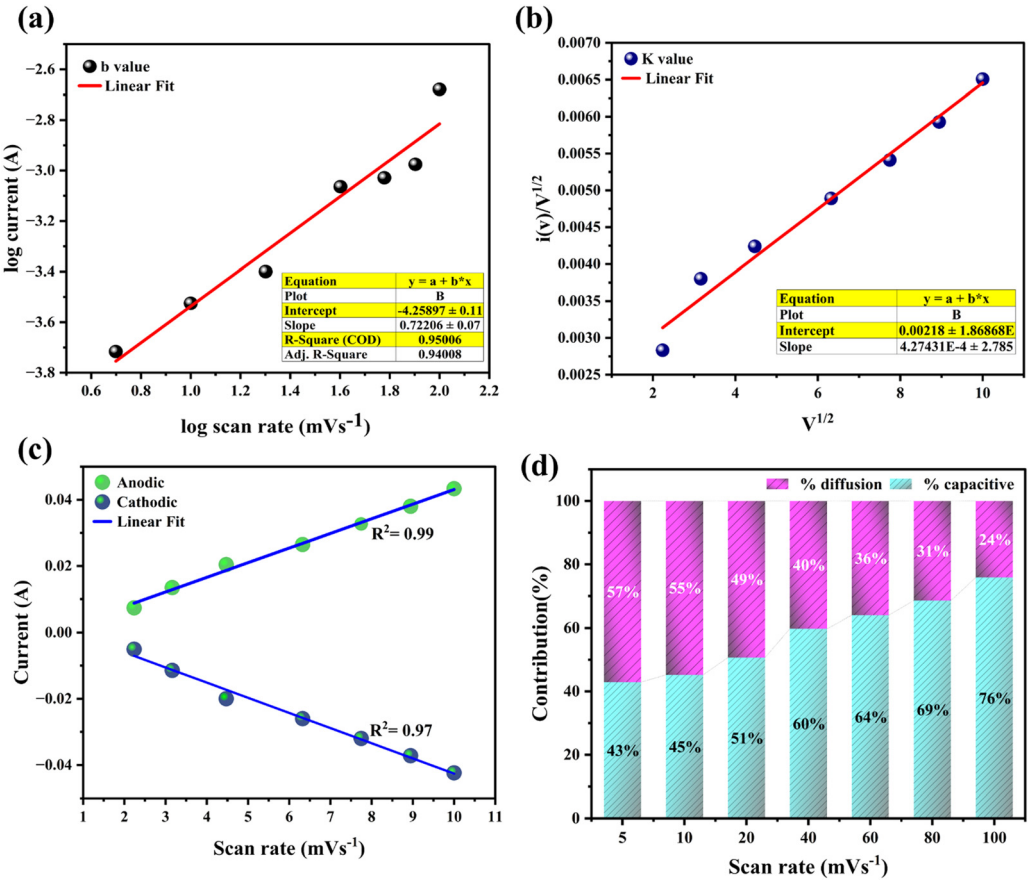

Fig. 7 (a) Logarithmic relationship between peak current and scan rate, (b) plot showing the determination of the *k* value, (c) determine the anodic and cathodic linear fit, (d) histogram illustrating the proportion of capacitive contributions at various scan rates.

within a custom range but also overlooks the regression analysis of the model equations to account for the prediction of response variables in untested temperatures. This prerequisite experimental matrix aids in the fabrication of flexible microsupercapacitors by screen-printing devices using only the conductive functional inks that encompasses Co_3O_4/rGO matrices synthesized at those calcination temperatures that produces good responses as per the model equations. Table 2 shows the response variables and capacity retention of Co_3O_4/rGO-550 microsupercapacitor and their comparison with other state-of-the-art microsupercapacitors that are reported in the literature.

5.1. Overall model obtained from RSM

A generalized quadratic polynomic model was chosen as shown in eqn (8) owing to its capability to rationalize the curvature in the response surface and to establish a relationship between the input factors and response variables when their dependence is not linear.

$$y_i = \beta_0 + \beta_1 x_1 + \beta_2 x_2 + \beta_{11} {x_1}^2 + \beta_{22} {x_2}^2 + \beta_{12} x_1 x_2 \quad (8)$$

Regression analysis fits the generalized model with the experimental data to yield the following model equations:

$$\text{Areal capacitance} = -0.00558714A^2 + 6.69706A - 1129.77 \quad (9)$$

$$\text{Energy density} = -0.000777143A^2 + 0.931457A - 157.273 \quad (10)$$

$$\text{Power density} = 0.00680786A^2 - 7.67134A + 4390.02 \quad (11)$$

From eqn (9)–(11), the conglomerative effect arising from the interactions of A and B are bypassed as indicated by the absence of the regression coefficient β_{12}. Also, it is coherent that the model avoids the inclusive effect of the linear coefficient β_2 and quadratic coefficient β_{22} due to the invariability of the CV cycles. It is observable that the square of the temperature negatively affects the microsupercapacitor performance in the case of areal capacitance and energy density. The coefficient of A^2 suggests a downward parabolic relationship, but the smaller magnitude in the case of energy density indicates a more gradual curvature compared to areal capacitance. The negative constant terms for areal capacitance and energy density can likely be considered a baseline point of reference and may not have any practical significance unless A could be 0. On the other hand, the linear temperature term was found to negatively impact the power density. However, the coefficient of A^2 suggests an upward (convex) parabolic relationship, indicating that power density decreases at lower temperatures but eventually increases as temperature rises. Meanwhile, the negative linear

© 2025 The Author(s). Published by the Royal Society of Chemistry

Open Access Article. Published on 10 de març 2025. Downloaded on 17/5/2026 14:58:41.
This article is licensed under a Creative Commons Attribution 3.0 Unported Licence.

Table 2 Summary table of the electrochemical performance metrics of microsupercapacitors reported in the literature

Electrode material	Areal capacitance, mF cm^{-2}	Capacity retention, %	Cycles	Energy density, μW h cm^{-2}	Power density, mW cm^{-2}	Ref.
Co_3O_4/rGO//AC	1220.2	91.7	10 000	343.51	3876.6	This work
Co_3O_4/rGO	939.0	94.6	10 000	130.4	2134.0	This work
Co-Al, $Ti_3C_2T_x$	40	92	10 000	8.84	0.23	38
V_2O_5, G-VNQD	58	65	8000	18.07	—	39
Graphene/AC	12.5	88.1	5000	1.07	4	40
N/rGO	3.4	98.4	2000	—	—	41
Ag/PPy	—	82.6	10 000	4.33	—	42
HRGO	40	83.5	10 000	5.4	—	43
AC	2381	78.9	10 000	331	—	44
$Ti_3C_2T_x$	2.337	93.1	10 000	—	3.74	45
ECG/SWCNT	7.7	>99	15 000	—	—	46
NiO	155	90	4000	—	—	47
$Cu_{0.56}Co_{2.44}O_4/MnO_2$, CNT	665.3	89.8	8000	182.3	2.3	48
(Cu, Co)Se_2, $Ti_3C_2T_x$	58	84	10 000	8.06	5	49
NiCoP/Ti_3C, AC	20	>90	5000	—	—	50
(Ni, Co)Se_2, $Ti_3C_2T_x$	63	92	10 000	8.75	0.5	51
MoS_2/EEG	13.6	90	10 000	1478	80	52
AC	454.1	85	3000	463.1	2–6.7	53
PEDOT:PSS/MnO_2	135.4	94	3000	12.03	32	54
MnO_2/Ti_3C_2	295	87	10 000	162	2.7	55
FGO/FrGO	7.3	98	5000	2.52	0.028	56
C/TiO_2	27.3	100	10 000	—	—	57
VN	210	>80	3000	2	10	58
WN	550	~100	1600	—	—	59
$V_3CrC_3T_x$, Zn	278.3	84.5	20 000	51.12	—	60
V_2O_5/CNT	18.98	95	10 000	5.93	0.0399	61

coefficient suggests that power density decreases as temperature increases up to a certain point. Quadratic terms are present in all three performance indicators, showing non-linear correlations with temperature. This is a characteristic in response surface modeling, wherein curvature and interactions are anticipated.[62,63] The influence of temperature variations on each metric is indicated by the magnitudes of the coefficients. Herein, compared to energy density and power density, areal capacitance is more sensitive to temperature fluctuations (as indicated by the greater linear coefficient). Since the number of CV cycles does not significantly impact the output parameters, the interaction between temperature and CV cycles (*i.e.* AB) was avoided in the model equations.

5.2. Analysis of variance (ANOVA) test

The statistical analysis of the data was carried out using ANOVA and the results are reported in Table S4 (ESI†). A *p*-value greater than 0.05 was obtained for the output parameters indicating that there is no significant statistical difference between the group means being compared. This could be due to the smaller number of trials conducted which leads to the false null hypothesis (Type II error) not being rejected at the 5% level. Nevertheless, the model exhibited predicted R^2 values of 0.8562, 0.8571, and 0.7892 for areal capacitance, energy density, and power density while demonstrating adjusted R^2 values of 0.7125, 0.7141, and 0.5985 respectively. The adjusted R^2 values are a measure of the model's potency to elucidate the variability in the experimental data while considering the quantified predictors in the model. This penalizes the inclusion of non-significant terms to account for the possibility of overfitting. On the other hand, the predicted R^2 values simply provide an estimate of the model's predictive abilities for new and unseen data through an internal cross-validation method. The disparity between the predicted R^2 value and the adjusted R^2 value falls within 0.2 for all the response variables suggesting a reasonable fit and a superlative predictive capability.

The model has 2 degrees of freedom for the regression, demonstrating that both factors A and B were analyzed. Despite the analysis, the lower adjusted R^2 value for power density suggests that some variability in the data might be due to CV cycles not being completely included in the model. In spite of not obtaining R^2 values over 90%, the model nonetheless elucidates a greater portion of the variance in the response variable. However, the relevance of the model was highlighted by the *F*-values as they demonstrated insignificance for areal capacitance and energy density. This was due to obtaining a *F*-value greater than 1 suggesting that the variability between the group means is larger than the variability within the groups, indicating that there are significant differences between the group means. For the case of power density, an *F*-value of 0.37 was reported for the temperature variable indicating that the response was insignificant for the changes in the activator (temperature). Regardless, the two-way interactions (*i.e.* AA) for all three output parameters reported *F* values greater than 1. From this, it could be concluded that the model predicted by D-optimal design fits the data reported experimentally.

Thus, ANOVA's results complement DoE from a statistical point of view. The innate tendency of ANOVA to confirm the reliability of the observed trends and ensure they are not a product of random variations in the experimental results, eases the consideration of operation conditions and materials for the fabrication of flexible devices. Additionally, the most important

Open Access Article. Published on 10 de març 2025. Downloaded on 17/5/2026 14:58:41.
This article is licensed under a Creative Commons Attribution 3.0 Unported Licence.

part of these statistical results are that they encourage reproducible improvements.

5.3. Analysis of DoE response profiles

Fig. S5 (ESI†) illustrates the main effects plots that display the impact of temperature on the three response variables. From the figure, one can observe the areal capacitance to be increasing as the temperature climbs from 350 °C to about 550 °C, where it hits its apex. Beyond 550 °C, it begins to deteriorate. This implies that the ideal temperature for areal capacitance is about 550 °C. Below this temperature, any increments in temperature enhance capacitance, presumably due to better electrochemical activity or other favourable material characteristics. However, beyond 550 °C, the capacitance declines, perhaps as a result of thermal degradation or other unfavourable effects on the structure of the material.[64] A similar profile was obtained for energy density where beyond 550 °C, the decrease in energy density raises the possibility that greater temperatures could cause stability or efficiency losses, either as a result of thermal degradation or modifications to the material's composition or morphology that impair its ability to store energy.[65] On the other hand, power density decreases initially as the temperature increases from 350 °C to 550 °C, reaching a minimum of 550 °C. Afterward, it begins to increase again as the temperature continues to rise to 750 °C. This profile substantiates that the power density is negatively impacted by rising temperatures up to 550 °C possibly due to the growing internal resistance.[66] However, beyond 550 °C, the increased power density could be attributed to the improved mobility of the ions leading to better conductivity. From Table S5 (ESI†), one can infer the interquartile range (IQR), which is the difference between the third and first quartile (*i.e.* Q3-Q1), that areal capacitance and power density have a relatively large IQR of 270.9 mF cm^{-2} and 252.2 mW cm^{-2} respectively while energy density has an IQR 37.65 μW h cm^{-2}. This highlights that the central 50% of the data are relatively more spread out for areal capacitance and power density indicating their sensitivity to changes in temperature. Meanwhile, energy density's IQR is more consistent across the middle range of conditions tested. The mean and median values are very close to each other for the three response variables illustrating a relatively symmetric distribution. The difference between the maximum and minimum values for areal capacitance is 385 mF cm^{-2} so having an IQR of 270.9 mF cm^{-2} seems consistent with the overall spread. Similarly, the differences in energy density and power density are 53.5 μW cm^{-2} and 384.1 mW cm^{-2} which satisfactorily encompasses their respective IQR values. This is demonstrated graphically with the help of a boxplot for the three response variables in Fig. S6 (ESI†) where all the response variables have no outliers due to the points falling within the whiskers. The median tends to be slightly lower than the IQR for areal capacitance and energy density implying a slight left skew despite the distribution being fairly symmetrical. On the other hand, power density appears to have a right skew.

The normal probability plots of the three response variables in Fig. S7(a)–(c) (ESI†), showcase the residuals following a straight line meaning the data points are normally distributed. However, the normal probability plot for power density follows a normal distribution with relatively more spread at the extremes, suggesting normality with some possible outliers. The *versus* fits for the response variables in Fig. S7(d)–(f) (ESI†). demonstrate a random scattering of the residuals which means the model fits the data well, with no serious violations of assumptions.

The histograms in Fig. S8 (ESI†) represent an even distribution of residuals with a broader spread. This could be due to a lesser number of trial runs.

In Fig. S7(g)–(i) (ESI†), the extent of variation of the residuals with no clear pattern can be incurred from the *versus* order plots of areal capacitance and energy density indicating no shortcomings regarding the independence of residuals. Though, power density's plot comparatively shows a bit more of a pattern, nothing concerning can be observed from it. Fig. S9 (ESI†) shows the response variables having *p*-values over 0.05 further supporting the discussions above regarding no deviations from normality while also enclosing all points within the 95% confidence interval.

5.4. Validation of model

As represented in Table S6 (ESI†), the responses predicted by the model are close to the reported values validating the strong fit of the model. To determine an optimal temperature for which satisfactory values of areal capacitance, energy density, and power density are attained, a response optimizer was used to generate optimization plots. The conditions specified in the input were to maximize all three output parameters for the temperature range between 350 °C and 750 °C. The model suggested 550 °C as the optimum temperature to experiment with a composite desirability of 0.86480 as depicted in Fig. S10 (ESI†).

Point confirmation was performed as a part of post-processing to further validate the reliability and pertinency of the model. This not only helps in verifying the proximity of the model's predictive capabilities with the experimental actuality but, also minimizes any uncertainties by proving the absence of the baseline null hypothesis. The responses obtained from post-processing help in confirming the 95% confidence interval's potency for future predictions. Since, an optimal temperature of 550 °C was suggested by the model, the ZIF-67/GO was synthesized again and calcinated at 550 °C to obtain a Co_3O_4/rGO matrix. A conductive nanocomposite ink was formulated with the matrix as per the aforementioned procedure, and the resulting ink was used for screen-printing an interdigitated asymmetric microsupercapacitor. Electrochemical characterizations of the fabricated device showed areal capacitance, energy density, and power density of 927.4 mF cm^{-2}, 128.6 μW h cm^{-2}, and 2202.1 mW cm^{-2} respectively which were in close proximity to the model predicted values of 863.503 mF cm^{-2}, 119.943 μW h cm^{-2}, and 2230.16 mW cm^{-2}. These values fell within the 95% confidence interval as presented in Table S7 (ESI†), indicating the experimental results are consistent with the model's predictions.[67] Additionally, it proves that the differences between the experimental and predicted responses are well within the expected range of random error.

© 2025 The Author(s). Published by the Royal Society of Chemistry

Open Access Article. Published on 10 de març 2025. Downloaded on 17/5/2026 14:58:41.
This article is licensed under a Creative Commons Attribution 3.0 Unported Licence.

6. Conclusion

In summary, the Co_3O_4/rGO nanocomposite with exceptional capacitive properties was successfully synthesized through a straightforward method. This involved using GO and ZIF-67 as precursors and applying simple calcination at various temperatures. ZIF-derived Co_3O_4 particles with a polyhedral structure were effectively distributed on the conductive rGO surface *via* a straightforward thermolysis process. We observed that varying annealing temperatures affected the material properties and their electrochemical performance in an interactive manner. As the temperature increased, both capacitive behaviour and electronic conductivity declined. Among all materials, Co_3O_4/rGO-550 °C demonstrated the best performance. In a symmetric capacitor with a 1 M KOH electrolyte, 550 °C achieved the highest areal capacitance of 939 mF cm^{-2}. This remark was concluded through both RSM and experimentation. The model predicted by RSM exhibited responses that were closely aligned with the experimental values indicating the accuracy of the model for the symmetric micro-supercapacitor in the 95% confidence interval. This enabled the employment of 550 °C as the optimal temperature for the fabrication and characterization of the asymmetric micro-supercapacitor.

Data availability

The datasets generated and/or analyzed during the current study are available from the corresponding author on reasonable request. All relevant data supporting the findings of this study, including experimental protocols, characterization data, and performance metrics, have been made available within the article and its ESI.† Any additional data required for replication or further inquiry can be obtained upon request, subject to the policies of our institution.

Conflicts of interest

The authors declare no conflict of interest.

Acknowledgements

Mohammad Saquib is grateful for the Dr T. M. A. Pai Fellowship from the Manipal Academy of Higher Education for his doctoral research.

References

1 Y.-Z. Zhang, Y. Wang, T. Cheng, L.-Q. Yao, X. Li, W.-Y. Lai and W. Huang, Printed supercapacitors: materials, printing and applications, *Chem. Soc. Rev.*, 2019, **48**, 3229–3264, DOI: **10.1039/C7CS00819H**.

2 M. Saquib, S. Shetty, M. Lakshmikanth, A. Rathod, K. Naik, R. Nayak and M. Selvakumar, Challenges in carbon ink formulation and strategies for fabrication of flexible supercapacitors, *Carbon Trends*, 2025, **19**, 100458, DOI: **10.1016/j.cartre.2025.100458**.

3 G. Wang, L. Zhang and J. Zhang, A review of electrode materials for electrochemical supercapacitors, *Chem. Soc. Rev.*, 2012, **41**, 797–828, DOI: **10.1039/C1CS15060J**.

4 X. Shi, S. Pei, F. Zhou, W. Ren, H. M. Cheng, Z. S. Wu and X. Bao, Ultrahigh-voltage integrated micro-supercapacitors with designable shapes and superior flexibility, *Energy Environ. Sci.*, 2019, **12**, 1534–1541, DOI: **10.1039/c8ee02924e**.

5 S. Bellani, E. Petroni, A. E. Del Rio Castillo, N. Curreli, B. Martín-García, R. Oropesa-Nuñez, M. Prato and F. Bonaccorso, Scalable Production of Graphene Inks via Wet-Jet Milling Exfoliation for Screen-Printed Micro-Supercapacitors, *Adv. Funct. Mater.*, 2019, **29**, 1–14, DOI: **10.1002/adfm.201807659**.

6 V. Shrivastav, S. Sundriyal, A. Kaur, U. K. Tiwari, S. Mishra and A. Deep, Conductive and porous ZIF-67/PEDOT hybrid composite as superior electrode for all-solid-state symmetrical supercapacitors, *J. Alloys Compd.*, 2020, **843**, 155992, DOI: **10.1016/j.jallcom.2020.155992**.

7 S. Shetty, M. Saquib, M. Selvakumar, H. Firouzi and R. Nayak, Graphene-enhanced manganese dioxide functional ink infused with polyaniline for high-performance screen-printed micro supercapacitor, *Mater. Res. Express*, 2024, **11**, 085503, DOI: **10.1088/2053-1591/ad674e**.

8 M. Saquib, R. Nayak, D. Devadiga, M. Selvakumar, S. Paramasivam, C. Ghosh, Y. N. Sudhakar and S. Senthilkumar, Printed flexible supercapacitor from conductive ink of graphite nanocomposite blended with Co_3O_4 to facilitate the fabrication of energy storage device, *J. Energy Storage*, 2023, **72**, 108800, DOI: **10.1016/j.est.2023.108800**.

9 M. Saquib, M. Selvakumar, R. Nayak, A. Prakash, Y. N. Sudhakar, S. Senthilkumar and D. K. Bhat, Formulation and optimization of Ni-MOF/CuSe nanocomposite ink for high-performance flexible microsupercapacitor, *J. Energy Storage*, 2024, **103**, 114230, DOI: **10.1016/j.est.2024.114230**.

10 M. K. Rao, M. Saquib, M. Selvakumar, M. G. Mahesha, S. Paramasivam, N. S. Prabhu, S. Senthilkumar and S. D. Kamath, Quasi 2D Ruddlesden–Popper perovskite thin film electrode for supercapacitor application: role of diffusion and capacitive process in charge storage mechanism, *FlatChem*, 2023, **41**, 100527, DOI: **10.1016/j.flatc.2023.100527**.

11 M. F. El-Kady and R. B. Kaner, Scalable fabrication of high-power graphene micro-supercapacitors for flexible and on-chip energy storage, *Nat. Commun.*, 2013, **4**, 1475, DOI: **10.1038/ncomms2446**.

12 N. Lei, Y. Qiao, G. Liu, R. Xu, G. Jiang, M. Demir and P. Ma, MnO_2 modified perovskite oxide $SrCo_{0.875}Nb_{0.125}O_3$ as supercapacitor electrode material, *Mater. Chem. Phys.*, 2022, **288**, 126389, DOI: **10.1016/j.matchemphys.2022.126389**.

13 J. R. Miller, R. A. Outlaw and B. C. Holloway, Graphene Double-Layer Capacitor with ac Line-Filtering Performance, *Science*, 2010, **329**, 1637–1639, DOI: **10.1126/science.1194372**.

14 H. Aydın, Ü. Kurtan, B. Üstün, S. N. Koç, E. Akgül and M. Demir, A preparation of niobium diboride (NbB2) via molten salt method: impact of boron concentration on the structural and electrochemical performance, *Mater. Res. Bull.*, 2024, **180**, 113062, DOI: **10.1016/j.materresbull.2024.113062**.

© 2025 The Author(s). Published by the Royal Society of Chemistry

Open Access Article. Published on 10 de març 2025. Downloaded on 17/5/2026 14:58:41.
This article is licensed under a Creative Commons Attribution 3.0 Unported Licence.

15 J. He, Y. Zhou, S. Wu, L. Jin, J. Cao, M. Demir and P. Ma, Cr-Substituted $SrCoO_{3-\delta}$ Perovskite with Abundant Oxygen Vacancies for High-Energy and Durable Low-Temperature Antifreezing Flexible Supercapacitor, *Inorg. Chem.*, 2024, **63**, 13755–13765, DOI: **10.1021/acs.inorgchem.4c02115**.

16 P. Simon and Y. Gogotsi, Capacitive Energy Storage in Nanostructured Carbon–Electrolyte Systems, *Acc. Chem. Res.*, 2013, **46**, 1094–1103, DOI: **10.1021/ar200306b**.

17 K. Qiu, Y. Lu, J. Cheng, H. Yan, X. Hou, D. Zhang, M. Lu, X. Liu and Y. Luo, Ultrathin mesoporous Co_3O_4 nanosheets on Ni foam for high-performance supercapacitors, *Electrochim. Acta*, 2015, **157**, 62–68, DOI: **10.1016/j.electacta.2014.12.035**.

18 M. Zhang, H. Fan, N. Zhao, H. Peng, X. Ren, W. Wang, H. Li, G. Chen, Y. Zhu, X. Jiang and P. Wu, 3D hierarchical $CoWO_4/Co_3O_4$ nanowire arrays for asymmetric supercapacitors with high energy density, *Chem. Eng. J.*, 2018, **347**, 291–300, DOI: **10.1016/j.cej.2018.04.113**.

19 N. Afsahi, M. Majumder and N. Naseri, Printed flexible solid-state microsupercapacitor with highly-stable aqueous cobalt-based inks, *Chem. Eng. J.*, 2024, **493**, 152356, DOI: **10.1016/j.cej.2024.152356**.

20 R. Xu, P. Liu, G. Ji, L. Gao and J. Zhao, Versatile Strategy to Design Flexible Planar-Integrated Microsupercapacitors Based on Co_3O_4-Decorated Laser-Induced Graphene, *ACS Appl. Energy Mater.*, 2020, **3**, 10676–10684, DOI: **10.1021/acsaem.0c01744**.

21 N. Liu, P. Tao, C. Jing, W. Huang, X. Zhang, M. Wu, J. Lei and L. Tang, A facile fabrication of nanoflower-like Co_3O_4 catalysts derived from ZIF-67 and their catalytic performance for CO oxidation, *J. Mater. Sci.*, 2018, **53**, 15051–15063, DOI: **10.1007/s10853-018-2696-3**.

22 M. Saquib, S. Shiraj, R. Nayak, A. Nirmale and M. Selvakumar, Synthesis and Fabrication of Graphite/WO_3 Nanocomposite-Based Screen-Printed Flexible Humidity Sensor, *J. Electron. Mater.*, 2023, **52**, 4226–4238, DOI: **10.1007/s11664-023-10404-y**.

23 G. P. Kuppuswamy, K. Pushparaj, V. J. Surya, E. K. Varadharaj, S. Senthil Kumar, C. Di Natale and Y. Sivalingam, A ZIF-67 derived Co_3O_4 dodecahedron shaped microparticle electrode based extended gate field-effect transistor for non-enzymatic glucose detection towards the diagnosis of diabetes mellitus, *J. Mater. Chem. C*, 2022, **10**, 5345–5355, DOI: **10.1039/D1TC05281K**.

24 V. Costa Bassetto, J. Xiao, E. Oveisi, V. Amstutz, B. Liu, H. H. Girault and A. Lesch, Rapid inkjet printing of high catalytic activity Co_3O_4/N-rGO layers for oxygen reduction reaction, *Appl. Catal., A*, 2018, **563**, 9–17, DOI: **10.1016/j.apcata.2018.06.026**.

25 T. Kim, G. Jung, S. Yoo, K. S. Suh and R. S. Ruoff, Activated Graphene-Based Carbons as Supercapacitor Electrodes with Macro- and Mesopores, *ACS Nano*, 2013, **7**, 6899–6905, DOI: **10.1021/nn402077v**.

26 A. Numan, N. Duraisamy, F. Saiha Omar, Y. K. Mahipal, K. Ramesh and S. Ramesh, Enhanced electrochemical performance of cobalt oxide nanocube intercalated reduced graphene oxide for supercapacitor application, *RSC Adv.*, 2016, **6**, 34894–34902, DOI: **10.1039/C6RA00160B**.

27 X. Qiao, S. Liao, C. You and R. Chen, Phosphorus and Nitrogen Dual Doped and Simultaneously Reduced Graphene Oxide with High Surface Area as Efficient Metal-Free Electrocatalyst for Oxygen Reduction, *Catalysts*, 2015, **5**, 981–991, DOI: **10.3390/catal5020981**.

28 R. Singaravelan and S. B. S. Alwar, Effect of reaction parameters in synthesis, characterisation of electrodeposited zinc nanohexagons, *J. Nanostruct. Chem.*, 2014, **4**, 109–117, DOI: **10.1007/s40097-014-0121-2**.

29 S. Visweswaran, R. Venkatachalapathy, M. Haris and R. Murugesan, Structural, morphological, optical and magnetic properties of sprayed NiO thin films by perfume atomizer, *Appl. Phys. A: Mater. Sci. Process.*, 2020, **126**, 524, DOI: **10.1007/s00339-020-03709-w**.

30 Y. Lü, W. Zhan, Y. He, Y. Wang, X. Kong, Q. Kuang, Z. Xie and L. Zheng, MOF-Templated Synthesis of Porous Co_3O_4 Concave Nanocubes with High Specific Surface Area and Their Gas Sensing Properties, *ACS Appl. Mater. Interfaces*, 2014, **6**, 4186–4195, DOI: **10.1021/am405858v**.

31 M. Zain, K. A. Yasin, S. Haq, W. Rehman, S. U. Din, S. Shujaat, A. Syed, M. K. Hossain, B. A. Paray, J. Razzokov and A. Samad, Effect of calcination temperature induced structural modifications on the photocatalytic efficacy of Fe_2O_3–ZrO_2 nanostructures: mechanochemical synthesis, *RSC Adv.*, 2024, **14**, 15085–15094, DOI: **10.1039/D4RA01944J**.

32 M. Panahi, M. Ghorbani and M. Soleimani Lashkenari, Construction of CO_3O_4 derived ZIF/GO electrode for outstanding stability in supercapacitors devices, *Int. J. Hydrogen Energy*, 2022, **47**, 9800–9809, DOI: **10.1016/j.ijhydene.2022.01.035**.

33 Y. Du, H. Zhao, H. Ji, W. Wang, H. Wang and F. Xu, Research on lubrication mechanism of plunger pair considering viscosity temperature and pressure effect, *Phys. Fluids*, 2024, **36**, 097119, DOI: **10.1063/5.0227691**.

34 J. W. Haverkort, A theoretical analysis of the optimal electrode thickness and porosity, *Electrochim. Acta*, 2019, **295**, 846–860, DOI: **10.1016/j.electacta.2018.10.065**.

35 M. Haque, Q. Li, A. D. Smith, V. Kuzmenko, P. Rudquist, P. Lundgren and P. Enoksson, Self-discharge and leakage current mitigation of neutral aqueous-based supercapacitor by means of liquid crystal additive, *J. Power Sources*, 2020, **453**, 227897, DOI: **10.1016/j.jpowsour.2020.227897**.

36 G. Maheshwaran, G. Seethalakshmi, V. Kousalya Devi, L. M. VenkataKrishna, M. Ramesh Prabhu, M. Krishna Kumar and S. Sudhahar, Synergistic effect of Cr_2O_3 and Co_3O_4 nanocomposite electrode for high performance supercapacitor applications, *Curr. Appl. Phys.*, 2022, **36**, 63–70, DOI: **10.1016/j.cap.2022.01.007**.

37 M. Z. Iqbal, S. Zakar, S. S. Haider, A. M. Afzal, M. J. Iqbal, M. A. Kamran and A. Numan, Electrodeposited CuMnS and CoMnS electrodes for high-performance asymmetric supercapacitor devices, *Ceram. Int.*, 2020, **46**, 21343–21350, DOI: **10.1016/j.ceramint.2020.05.230**.

38 S. Xu, Y. Dall'Agnese, G. Wei, C. Zhang, Y. Gogotsi and W. Han, Screen-printable microscale hybrid device based on MXene and layered double hydroxide electrodes for

© 2025 The Author(s). Published by the Royal Society of Chemistry

Open Access Article. Published on 10 de març 2025. Downloaded on 17/5/2026 14:58:41. This article is licensed under a Creative Commons Attribution 3.0 Unported Licence.

powering force sensors, *Nano Energy*, 2018, **50**, 479–488, DOI: 10.1016/j.nanoen.2018.05.064.

39 K. Shen, J. Ding and S. Yang, 3D Printing Quasi-Solid-State Asymmetric Micro-Supercapacitors with Ultrahigh Areal Energy Density, *Adv. Energy Mater.*, 2018, **8**(20), 1800408, DOI: 10.1002/aenm.201800408.

40 H. Chen, S. Chen, Y. Zhang, H. Ren, X. Hu and Y. Bai, Sand-Milling Fabrication of Screen-Printable Graphene Composite Inks for High-Performance Planar Micro-Supercapacitors, *ACS Appl. Mater. Interfaces*, 2020, **12**, 56319–56329, DOI: 10.1021/acsami.0c16976.

41 S. Liu, J. Xie, H. Li, Y. Wang, H. Y. Yang, T. Zhu, S. Zhang, G. Cao and X. Zhao, Nitrogen-doped reduced graphene oxide for high-performance flexible all-solid-state micro-supercapacitors, *J. Mater. Chem. A*, 2014, **2**, 18125–18131, DOI: 10.1039/C4TA03192J.

42 L. Liu, Q. Lu, S. Yang, J. Guo, Q. Tian, W. Yao, Z. Guo, V. A. L. Roy and W. Wu, All-Printed Solid-State Microsupercapacitors Derived from Self-Template Synthesis of Ag@PPy Nanocomposites, *Adv. Mater. Technol.*, 2018, **3**(1), 1700206, DOI: 10.1002/admt.201700206.

43 J. Yoo, S. Byun, C.-W. Lee, C.-Y. Yoo and J. Yu, Precisely Geometry Controlled Microsupercapacitors for Ultrahigh Areal Capacitance, Volumetric Capacitance, and Energy Density, *Chem. Mater.*, 2018, **30**, 3979–3990, DOI: 10.1021/acs.chemmater.7b03786.

44 Y. Liu, S. Zheng, J. Ma, Y. Zhu, J. Wang, X. Feng and Z.-S. Wu, Aqueous high-voltage all 3D-printed micro-supercapacitors with ultrahigh areal capacitance and energy density, *J. Energy Chem.*, 2021, **63**, 514–520, DOI: 10.1016/j.jechem.2021.08.018.

45 M. Yuan, L. Wang, X. Liu, X. Du, G. Zhang, Y. Chang, Q. Xia, Q. Hu and A. Zhou, 3D printing quasi-solid-state micro-supercapacitors with ultrahigh areal energy density based on high concentration MXene sediment, *Chem. Eng. J.*, 2023, **451**, 138686, DOI: 10.1016/j.cej.2022.138686.

46 J.-K. Chih, A. Jamaluddin, F. Chen, J.-K. Chang and C.-Y. Su, High energy density of all-screen-printable solid-state microsupercapacitors integrated by graphene/CNTs as hierarchical electrodes, *J. Mater. Chem. A*, 2019, **7**, 12779–12789, DOI: 10.1039/C9TA01460H.

47 P. Giannakou, M. G. Masteghin, R. C. T. Slade, S. J. Hinder and M. Shkunov, Energy storage on demand: ultra-high-rate and high-energy-density inkjet-printed NiO micro-supercapacitors, *J. Mater. Chem. A*, 2019, **7**, 21496–21506, DOI: 10.1039/C9TA07878A.

48 F. Li, M. Huang, J. Wang, J. Qu, Y. Li, L. Liu, V. K. Bandari, Y. Hong, B. Sun, M. Zhu, F. Zhu, Y. X. Zhang and O. G. Schmidt, On-chip 3D interdigital micro-supercapacitors with ultrahigh areal energy density, *Energy Storage Mater.*, 2020, **27**, 17–24, DOI: 10.1016/j.ensm.2020.01.008.

49 B. Balan, S. Ramasamy, S. P. Rajendra, M. S. AlSalhi and S. Angaiah, Advanced (Cu,Co)Se_2 Nanocubes and Ti-MXene Based Screen Printed Electrodes for High Performance Flexible Microsupercapacitors, *Adv. Funct. Mater.*, 2024, **34**(48), 2408639, DOI: 10.1002/adfm.202408639.

50 L. Yu, W. Li, C. Wei, Q. Yang, Y. Shao and J. Sun, 3D Printing of NiCoP/Ti_3C_2 MXene Architectures for Energy Storage Devices with High Areal and Volumetric Energy Density, *Nano-Micro Lett.*, 2020, **12**, 143, DOI: 10.1007/s40820-020-00483-5.

51 B. Balan, M. Narayanasamy, S. P. Rajendra, M. S. AlSalhi and S. Angaiah, Development of Penroseite (Ni,Co)Se_2 and Ti-MXene Inks for Maximizing the Energy Density of Screen-Printed Flexible Microsupercapacitor, *Adv. Mater. Technol.*, 2023, **8**(24), 2301329, DOI: 10.1002/admt.202301329.

52 W. Yang, Z. Hu, C. Zhang, Y. Guo and J. Zhao, Screen printing preparation of high-performance flexible planar micro-supercapacitors based on MoS_2 nanoparticles decorated electrochemically exfoliated graphene, *Electrochim. Acta*, 2022, **429**, 141041, DOI: 10.1016/j.electacta.2022.141041.

53 C. Gao, J. Huang, Y. Xiao, G. Zhang, C. Dai, Z. Li, Y. Zhao, L. Jiang and L. Qu, A seamlessly integrated device of micro-supercapacitor and wireless charging with ultrahigh energy density and capacitance, *Nat. Commun.*, 2021, **12**, 2647, DOI: 10.1038/s41467-021-22912-8.

54 D. Li, S. Yang, X. Chen, W. Lai and W. Huang, 3D Wearable Fabric-Based Micro-Supercapacitors with Ultra-High Areal Capacitance, *Adv. Funct. Mater.*, 2021, **31**(50), 2107484, DOI: 10.1002/adfm.202107484.

55 F. Zhao, W. Liu, T. Qiu, W.-B. Gong, W. Ma, Q. Li, F. Li and F. Geng, All Two-Dimensional Pseudocapacitive Sheet Materials for Flexible Asymmetric Solid-State Planar Microsupercapacitors with High Energy Density, *ACS Nano*, 2020, **14**, 603–610, DOI: 10.1021/acsnano.9b07183.

56 Y. Lu, Y. Zheng, H. Zhang, X. He, Q. Yang and J. Wu, A high performance and flexible in-plane asymmetric micro-supercapacitor (MSC) fabricated with functional electrochemical-exfoliated graphene, *J. Electroanal. Chem.*, 2020, **866**, 114169, DOI: 10.1016/j.jelechem.2020.114169.

57 J. Cai, C. Lv and A. Watanabe, High-performance all-solid-state flexible carbon/TiO 2 micro-supercapacitors with photo-rechargeable capability, *RSC Adv.*, 2017, **7**, 415–422, DOI: 10.1039/C6RA25136F.

58 K. Robert, C. Douard, A. Demortière, F. Blanchard, P. Roussel, T. Brousse and C. Lethien, On Chip Interdigitated Micro-Supercapacitors Based on Sputtered Bifunctional Vanadium Nitride Thin Films with Finely Tuned Inter- and Intracolumnar Porosities, *Adv. Mater. Technol.*, 2018, **3**(7), 1800036, DOI: 10.1002/admt.201800036.

59 S. Ouendi, K. Robert, D. Stievenard, T. Brousse, P. Roussel and C. Lethien, Sputtered tungsten nitride films as pseudocapacitive electrode for on chip micro-supercapacitors, *Energy Storage Mater.*, 2019, **20**, 243–252, DOI: 10.1016/j.ensm.2019.04.006.

60 H. Wang, Y. Xue, X. Song, S. Lei, H. Yu, C.-F. Du, Z. Ren, R. Guo and F. Zhou, Solid solution reinforced $V_3CrC_3T_x$ MXene cathodes for Zn-ion micro-supercapacitors with high areal energy density and superior flexibility, *J. Mater. Chem. A*, 2022, **10**, 20953–20963, DOI: 10.1039/D2TA04747K.

61 K.-W. Kim, K. Wu, B. Park, J. Jang, J. H. Kwon, A. Alam, S. Lim, S. H. Kim, J. K. Kim and H. C. Moon, 3D-printed,

Open Access Article. Published on 10 de març 2025. Downloaded on 17/5/2026 14:58:41.
This article is licensed under a Creative Commons Attribution 3.0 Unported Licence.

high-energy-density, current collector-free flexible micro-supercapacitors based on CNT@V_2O_5 nanowires, *J. Energy Storage*, 2024, **75**, 109642, DOI: **10.1016/j.est.2023.109642**.

62 S. Gite, R. S. Ambekar, S. B. A. Aaditya, S. Joshi and P. B. Karandikar, Analysis of asymmetrical supercapacitor with horizontally configured electrodes, *J. Energy Storage*, 2023, **68**, 107829, DOI: **10.1016/j.est.2023.107829**.

63 D. Jha, V. N. Karkaria, P. B. Karandikar and R. S. Desai, Statistical modeling of hybrid supercapacitor, *J. Energy Storage*, 2022, **46**, 103869, DOI: **10.1016/j.est.2021.103869**.

64 P. B. Karandikar, D. B. Talange, U. P. Mhaskar and R. Bansal, Development, modeling and characterization of aqueous metal oxide based supercapacitor, *Energy*, 2012, **40**, 131–138, DOI: **10.1016/j.energy.2012.02.020**.

65 M. Biswal, A. Banerjee, M. Deo and S. Ogale, From dead leaves to high energy density supercapacitors, *Energy Environ. Sci.*, 2013, **6**, 1249, DOI: **10.1039/c3ee22325f**.

66 C. Liu, Z. Yu, D. Neff, A. Zhamu and B. Z. Jang, Graphene-Based Supercapacitor with an Ultrahigh Energy Density, *Nano Lett.*, 2010, **10**, 4863–4868, DOI: **10.1021/nl102661q**.

67 S. Prakash, S. Naina Mohamed, S. G. Siddanth and K. Ponnusamy, Enhanced performance of novel microbial desalination cell using sago effluent as an anolyte: a response surface optimization approach, *J. Water Process Eng.*, 2024, **59**, 105004, DOI: **10.1016/j.jwpe.2024.105004**.

© 2025 The Author(s). Published by the Royal Society of Chemistry